Underneath the fascinations of carbon nanotubes and graphene nanoribbons

Wei-Tao Zheng[a] and Chang Q Sun†[bc]

As a new class of materials, carbon nanotubes (CNTs) and graphene nanoribbons (GNRs) have been continuing fascinating the community with properties that can be seen from neither bulk graphite nor diamond. Although the physics and chemistry of these carbon allotropes have been intensively investigated from various perspectives, the laws governing the fascinations and their interdependence remain as yet undetermined. From the perspectives of bond and nonbond formation, dissociation, relaxation, vibration, and the associated energetics and dynamics of charge repopulation, polarization, densification, and localization, this article aims to show that the broken-bond-induced local bond contraction and bond strength gain, quantum entrapment and densification of charge and energy, polarization of the unpaired edge dangling σ-bond electrons, and the formation of the pseudo-π-bond between the dangling σ-bond electrons along the edges are responsible for the anomalies. Theoretical reproduction of the experimentally observed elastic modulus enhancement, melting point depression, layer-number, strain, pressure and temperature induced Raman shift, C 1s core-level positive shift, work function reduction, band gap expansion, edge and defect selective generation of the Dirac-Fermi polarons and the associated magnetism consistently confirmed that the shorter and stronger bonds between undercoordinated carbon atoms modulate locally the atomic cohesive energy, the Hamiltonian, and hence the detectable bulk properties. The polarization of the unpaired dangling σ-bond electrons by the densely, deeply, and locally entrapped core and bonding electrons generates the massless, magnetic and mobile Dirac-Fermi polarons at sites surrounding vacancies and zigzag-GNR edges. The pseudo-π-bond formation between the nearest dangling σ-bond electrons along the armchair-GNR and the reconstructed zigzag-GNR edges discriminates them from the zigzag-GNR edges or vacancies in the electronic and magnetic properties. Consistency between predictions and observations confirmed that the C–C bond contracts by up to 30% with a 152% bond strength gain at the edges with respect to those in the bulk diamond.

[a]School of Materials Science, Jilin University, Changchun, 130012, China. E-mail: WTZheng@jlu.edu.cn
[b]Center for Coordination Bond-Band Engineering, School of Electrical and Electronic Engineering, Nanyang Technological University, Singapore, 639798, Singapore
[c]Institute for Quantum Engineering and Micro-Nano Energy Technology and Key Laboratory of Low-Dimensional Materials and Application Technologies, Faculty of Physics, Xiangtan University, Hunan, 411105, China. E-mail: ecqsun@ntu.edu.sg
† Associated with honorary appointments at Jilin and Xiangtan Universities.

I Introduction

- *CNTs and GNRs have fascinated the community with the conventionally-unexpected properties for two decades with undetermined mechanism underneath.*
- *Interaction between undercoordinated atoms and the local charge distribution in the valence band and above are the keys to the anomalies.*
- *Undercoordination induced local bond relaxation, quantum entrapment, and the polarization of the nonbonding charge should be the starting point of exploration.*

Broader context

Although the chemistry and physics of carbon nanotubes (CNTs) and graphene nanoribbons (GNRs) have been intensively investigated, the laws governing the fascinations remain as yet undetermined. From the perspectives of bond and nonbond formation, dissociation, relaxation, vibration, and the associated energetics and dynamics of charge repopulation, polarization, densification, and localization, we show that the broken-bond-induced local bond contraction and strength gain, quantum entrapment and densification of charge and energy, polarization of the unpaired dangling σ-bond electrons, and the formation of the pseudo-π-bond between the edge electrons originate the anomalies. Theoretical reproduction of the experimentally-observed elastic enhancement, thermal stability depression, C 1s core-level positive shift, work function reduction, band gap expansion, edge discriminative generation of the Dirac-Fermi polarons consistently confirmed that the shorter and stronger bonds between undercoordinated atoms modulate locally the atomic cohesive energy, the Hamiltonian, and hence the detectable bulk properties. The polarization of the unpaired nonbonding electrons by the densely and locally entrapped core and bonding electrons generates, however, the massless, magnetic, and mobile Dirac-Fermi polarons at sites surrounding vacancies and zigzag-GNR edges. The pseudo-π-bond formation between the nearest edge electrons of the AGNR and the reconstructed-ZGNR discriminates them from the zigzag-GNR edges or vacancies in the electronic and magnetic properties.

This journal is © The Royal Society of Chemistry 2011

Energy Environ. Sci., 2011, **4**, 627–655 | 627

1.1 Key identities of CNTs and GNRs

Since the discovery of carbon nanotubes (CNTs) in earlier 1990s,[1] there has been ever-increasing interest in the new forms of carbon because of not only the novel structures and properties that the bulk graphite or diamond do not demonstrate but also the potentially important applications in scientific and engineering thrusts such as atomic-force microscope tips,[2] cathode field emitters,[3,4] electronic circuit devices,[5,6] hydrogen storage,[7–10] chemical sensors,[11,12] energy storage and management.[13–16]

Unrolling a single-walled CNT (SWCNT) generates a graphene nanoribbon (GNR)[17,18] with high fraction of under-coordinated carbon atoms located at the open edges. The undercoordinated edge atoms and the abnormal performances of electrons surrounding the edges have inspired even more increasing interest because of the edge-associated intriguing phenomena. The edge associated anomalies can be seen from neither the SWCNTs nor the infinitely large graphene sheets (LGSs).[19–27]

Graphene is a wonder material with many superlatives to its name. It is the thinnest known material in the universe and the strongest ever measured. Its charge carriers or Dirac fermions (we call them Dirac-Fermi polarons as will be justified in later section) exhibiting giant intrinsic mobility can travel for micrometres without scattering at room temperature. Graphene can sustain current densities six orders of magnitude higher than that of copper, shows record thermal and electric conductivity, is impermeable to gases, and reconciles such conflicting qualities as brittleness and ductility. Serving as vehicles for the quantum spin Hall-effect in topological insulators,[24,28–34] Dirac-Fermi polarons[35,36] exhibit unique electrical supercurrent properties[37] on account of its reduced dimensionality and "relativistic" band structure.[38] When contacted with two superconducting electrodes, graphene can support Cooper pair transport, resulting in the well-known Josephson effect.[39] Scanning tunneling microscopy/spectroscopy (STM/S) measurements[40–42] have uncovered the Dirac-Fermi polarons as high protrusions in image and as sharp resonant peak at E_F in spectrum from sites surrounding
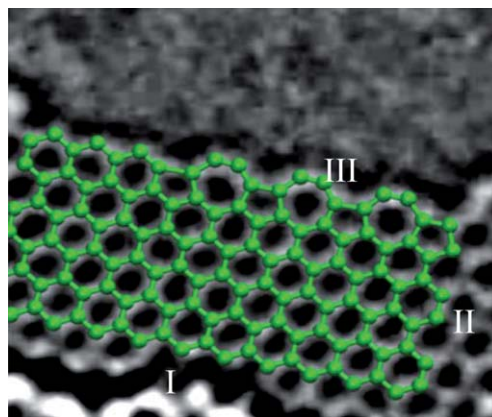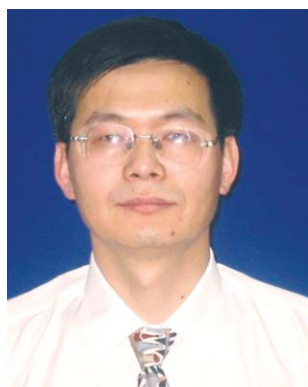

Fig. 1 STM image of a GNR with three types of edges: I: ZGNR edge with identical ($\sqrt{3}d$) atomic distance, II: AGNR edge with the alternative d and 2d atomic distances, and III: rec-ZGNR with atomic distances being similar to that of the AGNR.[46,63] The ZGNR edge generates Dirac fermions with magnetic and metallic nature while the AGNR and rec-ZGNR edges are the otherwise.

atomic vacancies, the edges of monolayer graphite terrace and graphene nanoribbons.[43–46] These polarons demonstrate anomalies including the extremely low effective mass,[47] extremely high group velocity, and a net ½ spin,[48,49] following the Dirac equation, and a nearly linear dispersion (Dirac cone) with energies crossing Fermi energy.[24,28–31,50–57] Electron transport in graphene allows the investigation of relativistic quantum phenomena in a bench top experiment. These phenomena and the strip-width-induced band gap expansion demonstrated by the AGNR can never be observed in the SWCNT, graphene or graphite crystal.[20,58]

There are typically three types of GNRs according to their chirality or shapes of edges: the zigzag- (I: ZGNR), the armchair- (II: AGNR), and the reconstructed- (III: rec-ZGNR) edges, as indicated in Fig. 1. Compared with LGSs or CNTs, the ZGNRs and vacancies share the hexagonal-sublattice possessing

Professor Wei-Tao Zheng received his PhD at Jilin University, China, in condensed matter physics in 1990. He visited Linköping University, Sweden in 1997, Chiba Institute of Technology, Japan in 1999, and Nanyang Technological University, Singapore in 2002, as visiting Professor. He has been working on superhard thin films, carbon and metal nitrides, and carbon-related nanomaterials such as CNTs, graphene, nanodiamond and their modifications, etc, both experimentally and computationally.

Wei-Tao Zheng

Chang Q Sun, received his PhD in 1996 at Murdoch University, Australia. With research interests in surface, interface, and low-dimensional physics and chemistry, CQ Sun has been working on very-low-energy electron diffraction and STM/S analysis of C, N, and O chemisorption bonding dynamics, size dependence of nanostructures, and thermo-mechanical behavior of low-dimensional systems with the development of the bond order-length-strength correlation theory, the local bond averaging approach, and the photoelectron residual spectroscopic technology.

Chang Q Sun

strongly-localized edge states[59] with magnetic and metallic nature, whereas the AGNRs have larger band gap (E_G) with semiconducting nature. The E_G of the AGNR is found roughly proportional to the inverse width of the GNRs.[48,60–62] The rec-ZGNR shares considerable similarity to that of the AGNR. One may note the difference between these edges is the distances between atoms along the outermost-edge. The atomic distance at the ZGNR edge is periodic with $\sqrt{3}d$ but at the AGNR the distance is d and 2d alternatively. A SWCNT can be viewed as a LGS without edges though the rolling of the GNR may introduce some slight strains.

1.2 Challenges and objectives

Overwhelming experimental efforts have been exerted primarily in the CNTs and GNRs growth, characterization, and functioning for practical applications. Considerable theoretical efforts have been made on the performance of the Dirac fermions that follow the relativistic Dirac equations and the energetic and structural optimization. However, physical insight into the origin behind the fascinations and their interdependence of the CNTs and the GNRs remain challenging. Opening questions may be exampled as the following:

i) GNRs and CNTs are mechanically stronger yet chemically and thermally less stable. CNTs exhibit extremely high strength yet relatively lower chemical and thermal stability compared to their bulk counterparts. Compared with the bulk value of 1.05 TPa, the elastic modulus of the SWCNT was measured to vary from 0.5 to 5.5 TPa depending on the presumption of the wall thickness of the CNT.[64–71] The Young's modulus of the multi-walled CNTs (MWCNTs) drops with the inverse wall thickness and is less sensitive to the outermost radius of the MWCNTs if the wall thickness remains unchanged.[72,73] Atoms in the open edge of a SWCNT coalesce at 1593 K[74] and a ~280% extensibility of the CNT occurs at ~2000 K.[75] Under the flash of an ordinary camera, the SWCNT burns under the ambient conditions.[76] Generally, for bulk materials, the elastic modulus is always proportional to the melting point.[77] The mechanism behind the paradox of elastic enhancement and T_m suppression of the CNTs is still a puzzle.

ii) The wall thickness, the C–C bond length and energy, and the role of atomic undercoordination remain a challenge. The wall thickness and the Young's modulus of the C–C bond in the SWCNTs are correlated, which leads to the uncertainty in both quantities. Although the atoms that surround defects or are located at the tip ends or at the surface are expected to play some unusual, yet unclear, roles in dominating the mechanical and thermal propertied of the CNTs and GNRs. A consistent insight into the mechanism behind the fascinations from the perspective of under-coordination is necessary.

iii) Mechanisms for the metallic and magnetic ZGNR and the semiconductive AGNR remain unclear. Compared with the LGS or CNTs, the ZGNRs possess strongly-localized edge states[59] with magnetic and metallic nature, whereas the AGNRs have a larger band gap (E_G) with semiconductive nature. The E_G is roughly proportional to the inverse width of the GNRs.[60–62] However, discrepancy remains between the theory and the experimentally derived E_G of GNR. Measurements[61] and theoretical calculations[48,62,78] showed less consistence in the band gap

opening of GNR. Mechanisms remain yet unclear regarding the generation of the localized edge states and the expansion trends of the E_G in spite of the possible mechanisms such as doping,[79] defects forming,[48,80,81] symmetry breaking,[82] substrate interaction,[83] edge distortion,[60] strain,[84] quantum confinement[45] and the staggered sublattice potentials modulation.[85]

iv) The mechanism of the edge selective generation and hydrogen annihilation of the Dirac fermions remains open. The Dirac-Fermi polarons[40–42] generate at sites surrounding atomic vacancies, the edges of monolayer graphite terrace and the ZGNRs,[43–46] other than the edges of the AGNR or the rec-AGNR. It remains unclear why the edge and site discriminate the generation of Dirac fermions.

v) Origin of and correlation between the positive C 1s core level shift of the GNR edge, GNR interior and the associated work function reduction with the number of GNR layers are ambiguous. Three XPS C1s components have been resolved from graphene flakes produce,[86] corresponding, respectively, from lower (larger value) to higher binding energies, to the contributions from the GNR edge, the mono-layer GNR or the surface of the triple-layered graphene, and the bulk graphite in multi-layered graphene. The C1s spectrum of the multilayered graphene is dominated by the surface and the bulk components while the spectra for the mono- and the triple-layers are dominated by the surface and edge components. It has been found[87] from the epitaxial few-layer graphene that the work function decreases from 4.6 to 4.3 eV and that the C1s core level shifts positively from 284.42 to 284.83 eV simultaneously when the number of graphene layers is decreased from ten to one, which is consistent with the reported thickness dependence of the Dirac point energy. The same thickness trend has also been observed from the C_{60}.[88] Unfortunately, few theoretical models have been available to account for the origin and interdependence of the coordination-resolved C 1s binding energy shift and the associated work function reduction.

vi) When the layer-number, strain, temperature, and pressure change, the vibration frequencies of the GNRs shift; formulation of the lattice dynamics is necessary.

vii) The common origin of these anomalies and their interdependence needs to be established. The difference between the graphite and the GNRs or the CNTs is nothing more than atomic coordination reduction that could be the point of starting. From the observation of the atomic dynamics of carbon at the edge of a hole in a suspended, single atomic layer of graphene, Girit et al.[46] found that the bonds rearrange and carbon atoms are ejected by the energetic electron beam as the vacancy hole grows. They observed the edge reconstruction and the stability of the "zigzag" edge configuration, revealing the complex behavior of atoms preferentially occurring at the boundary. Therefore, atomic coordination reduction and its consequences on the bond length, bond energy, and the associated electronic dynamics should be the origin of the anomalies and their interdependence.

In order to harness the GNRs and CNTs, we have to get these concerns be understood. It should be clear what the advantages are and what the limitations would be, and how to make use of the advantages and to overcome the limitations in practical applications. In fact, the properties of a substance are determined by the process and consequences of bond and nonbond formation, dissociation, relaxation and vibration, and the associated

energetics and dynamics of charge repopulation, polarization, densification, and localization.[89] From this perspective, this article attempts to address the above challenging issues by reporting the progress we made in recent years focusing on the fundamentals behind the fascinations and their interdependence. It is demonstrated that the atomic-undercoordination-induced local bond contraction and quantum entrapment, the polarization of the unpaired dangling σ-bond sp^2 electrons by the entrapped core and bond charges at the atomic vacancy and the ZGNR edges, and the formation of the pseudo-π-bond between the nearest dangling σ-bond electrons along the AGNR and the rec-ZGNR edges result in the fascinations. Theoretical reproduction of the experimentally observed elastic modulus enhancement, melting point depression, C 1s core-level shift, band gap expansion, edge and defect Dirac-Fermi polarons

relaxation. The key idea of the BOLS is that if one bond breaks, the remainders become shorter and stronger. The broken-bond-induced local strain and quantum entrapment cause strong localization and densification of charge, energy, and mass at sites surrounding atomic vacancies, defects, adatoms, terrace edges, and surfaces of various curvatures, resulting in perturbation to the atomic cohesive energy, electroaffinity, Hamiltonian, etc., and associated properties of a substance. This theory has resulted in discoveries of the common factors dictating the size dependency of nanostructures and enabled the unification of the size dependency of nanostructures in mechanical strength, thermal and chemical stability, lattice acoustic dynamics, photonic, electronic, magnetic and dielectric properties and their interdependence.[90]

The BOLS correlation is expressed as follows:[90,94]

$$\begin{cases} c_z & = d_i/d = 2/\{1 + \exp[(12 - z)/(8z)]\} & \text{(bond strain coefficient)} \\ c_z^{-m} & = E_i/E_b & \text{(bond strength)} \\ c_z^{-(m+\tau)} & = E_{id}/E_{bd} & \text{(binding energy density)} \\ z_{zb}c_z^{-m} & = E_{Ic}/E_{Bc} & \text{(atomic cohesive energy)} \end{cases} \tag{1}$$

generation and the associated magnetism will be demonstrated, which consistently confirmed that the shorter and stronger bonds between undercoordinated carbon atoms modulate locally the atomic cohesive energy and the Hamiltonian which alter the detectable bulk properties. The polarization of the unpaired sp^2 electrons by the densely, deeply, and locally entrapped core and bonding electrons generates the massless, magnetic and mobile Dirac-Fermi polarons at sites surrounding defects and ZGNR edges. The pseudo-π-bond formation at edges discriminates the AGNR and the rec-ZGNR from the AGNR in the electronic and magnetic anomalies.

II Principles

• *Atomic undercoordination induces local bond contraction and strength gain, quantum entrapment and densification of charge and energy, and nonbonding electron polarization.*
• *The BOLS provides perturbation in the Hamiltonian and the cohesive energy, which dominates the change of the observable bulk properties and their interdependence.*
• *The polarization of the dangling σ-bond sp^2 electrons at vacancy and ZGNR edges originates the anomalies of the magnetic, massless, metallic and mobile Dirac-Fermi polarons as carriers for quantum spin Hall Effect.*
• *The pseudo-π-bond formation between the nearest dangling bond sp^2 electrons along the outermost AGNR and rec-ZGNR edges makes them different from the vacancy and ZGNR.*

2.1 Undercoordinated bond strain and strengthening

2.1.1 BOLS: Quantum entrapment and densification. In order to cope with the undercoordinated systems, we have developed the bond-order-length-strength (BOLS) correlation mechanism[90] by extending the "atomic coordination – radius" correlation premise of Goldschmidt,[91] Pauling,[92] and Feibelman[93] to include the energetics and electronics of the spontaneous process of bond

where τ is the dimensionality, $z_{zb} = z/z_b$ is the reduced atomic CN with $z_b = 12$ being the bulk standard. The effective z values for a C atom in an isolated state and in the bulk of a diamond are 0 and 12, respectively. The atomic CN for diamond is 12 instead of 4 because the diamond structure is an interlock of two fcc structures.[95] The bond nature indicator for carbon, m, has been optimized to be 2.56. The CN for a C atom at the open edge of a graphene or a SWCNT is 2; in the interior of graphene or SWCNT it is 3; at a plane surface of a bulk diamond, the effective CN is 4. With the known C–C bond lengths of 0.154 nm for diamond and 0.142 nm for graphite, one can derive the effective CN for graphite as 5.335, according to the bond strain coefficient (eqn (1)). Fig. 2a illustrates the BOLS correlation at the GNR edge with the lattice strain and the potential well depression.[96]

2.1.2 Energy density *vs* atomic cohesive energy. According to the local bond averaging approach,[94] any detectable quantities of a bulk can be connected directly to the identities (nature, order, length, strength) of a representative bond for the specimen and the response of these identities to the applied stimulus such as the coordination environment, pressure, temperature. *etc.* With
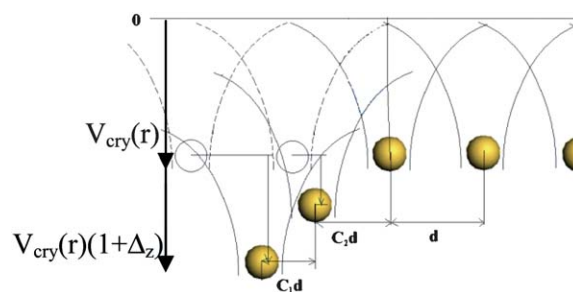

Fig. 2 Schematic illustration of the BOLS derived GNR edge bond strain (C_zd) and potential well depression from the bulk $V_{cry}(r)$ to $[V_{cry}(r)(1 + \Delta_z)]$ with Δ_z being the Hamiltonian perturbation.

a given interatomic potential, one can derive that the binding energy per unit volume determines the elastic modulus and the yield strength at an atomic site,[97]

$$\begin{cases} B = -v\dfrac{\partial^2 u(r)}{\partial v^2}\Big|_{r=d_z} \propto E_b d^{-3} & \text{(Bulk modulus at equilibrium)} \\ P = -\dfrac{\partial u(r)}{\partial v}\Big|_{r\neq d} \propto u(r) r^{-3} & \text{(Stress at non-equilibrium)} \end{cases}$$
(2)

The difference between the elastic modulus and the yield strength in definition is that the former is the second derivative of the potential at the equilibrium while the latter the first derivative at a critical r of plastic deformation. These two quantities share in the same dimension of energy density but they are different in physical meanings. Therefore, simply relating the elastic modulus to the plastic yield strength is questionable.

Likewise, the critical temperature for phase transition such as solid–solid, ferromagnetic–paramagnetic, melting and evaporating at a specific atomic site is proportional to the atomic cohesive energy, being the product of the cohesive energy per bond and the total number of bonds of the specific atom:[98]

$$T_{Ci} \propto z_i E_i$$
(3)

It has also been derived that the Raman shift is expressed as:[99]

$$\omega_i \propto \frac{z_i}{d_i}\left(\frac{E_i}{\mu}\right)$$
(4)

where μ is the reduced mass of the pair of bonding atoms.

2.1.3 Hamiltonian perturbation *vs* band engineering. According to the energy band theory,[100] the coupling of the interatomic potential, $V_{cry}(r)$, and the respective Bloch wave functions, being proportional to the mean cohesive energy per bond at equilibrium, $\langle E_b \rangle$, determine the energy band identities as the common origin such as the gap between the conduction and the valence band in semiconductors, E_G, energy dispersions, and the energy shift, $\Delta E_v(12) = E_v(12) - E_v(0)$, of a specific vth core band from that of an isolated atom, $E_v(0)$. The single-body Hamiltonian, H, and the related band identities are given as,[90]

$$\begin{cases} H & = -\dfrac{\hbar^2 \nabla^2}{2m} + V_{atom}(r) + V_{cry}(r) & \text{(Hamiltonian)} \\ E_G(12) & = 2|V_h| \propto \langle E_0 \rangle & \text{(Band-gap)} \\ E_v(12) & = E_v(0) - \alpha - t\sum{}' e^{ik\cdot R_j} & \text{(Energy-dispersion)} \\ E_v(0) & = \langle v, i|V_{atom}(r)|v, i\rangle & \text{(Core-level-energy)} \\ \alpha & = \langle v, i|V_{cry}(r)|v, i\rangle \propto \langle E_b \rangle & \text{(Exchange-Integral)} \\ t_{ij} & = \langle v, i|V_{cry}(r)|v, j\rangle \propto \langle E_b \rangle & \text{(Overlap-Integral)} \\ \Delta E_v(12) & = \alpha + z_b t \propto \langle E_b \rangle & \text{(Core-level-shift)} \\ \Delta E_v & \approx t\sum{}' e^{ik\cdot R_j} \propto \langle E_b \rangle & \text{(Band-width)} \end{cases}$$
(5)

The intra-atomic trapping potential, $V_{atom}(r)$, determines the value of $E_v(0)$. The crystal potential for an extended solid, $V_{cry}(r)$, determines the core level shift, $\Delta E_v(12) = E_v(12) - E_v(0)$ and the band width. It is stressed that the $E_v(0)$ and its bulk shift keep constant under any circumstances. The $\langle v, i| \ (i \neq j)$ is the specific

Bloch wave function for an atom at a specific site i. Because of the strong localization of the tight binding electrons in the inner shells, $\langle v, i|v, j\rangle = \delta_{ij}$. The value of t is much smaller than α. From the XPS spectrum bulk component whose maximal width is $2z\alpha$ (0.1–1.0 eV level), one can estimate that the t is in $<10^{-(1\sim2)}$ eV order.[101] The α is in the 10^0 eVs level. Therefore, the BE shift is dominated by α and is proportional to the bond energy, E_b. The E_G depends uniquely on the Fourier coefficient of the periodic crystal potential $V_{cry}(r)$, $|V_h|$. The k is the wave vector. Hence, the chemical bond, crystal potential, and the energy band structure can thus be correlated.

Incorporating the BOLS to the band theory, one can obtain the broken-bond-induced perturbation Δ_z to the interatomic potential in the Hamiltonian at the z-coordinated C atomic site:

$$\begin{cases} V_{cry} = V_{cry}(1 + \Delta_z) \\ \Delta_z = C_z^{-m} - 1 \end{cases}$$
(6)

This perturbation leads to the band gap expansion and core level shift, upon the undercoordinated atoms being involved.[90,102–104] Therefore, a measured XPS spectrum can be decomposed into component Gaussian peaks with each component corresponding to a particular value of z, as illustrated in Fig. 3. The intensities of the components are subject to the detectable fraction of the specifically z-coordinated atoms and the energy values of the peaks satisfy the constraint:

$$\frac{E_{1s}(z) - E_{1s}(0)}{E_{1s}(12) - E_{1s}(0)} = \frac{E_z}{E_b} = C_z^{-2.56}$$
(7)

Any perturbation such as bond relaxation caused by undercoordination and band nature alteration by compound or alloy formation to the $V_{cry}(r)$ or to the mean bond energy $\langle E_b \rangle$ will modulate the entire band structure and related properties of the given specimen. A geometric orientation alteration of a surface changes the effective CN slightly[105–107] but such alteration could change neither the E_G nor the $\Delta E_v(k)$ of the monolayer graphene. One can modify the bond energy by applying bond nature alteration through a chemical reaction or by applying bond
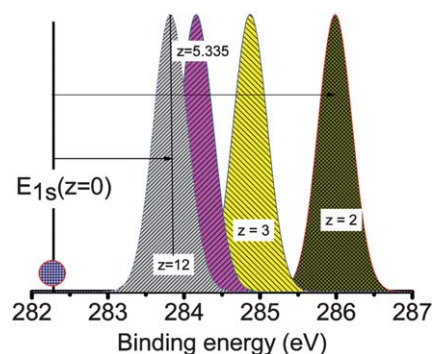

Fig. 3 Illustration of the atomic-CN-resolved C1s energy shift that can be decomposed into components corresponding to the specific atomic CNs. Lowered CN derives positive C1s energy shift. The intensities of the spectral components are determined by the detectable fractions of the z-coordinated atoms in the specimen. The energy between the specific component (z) and the $E_{1s}(0)$ depends on the cohesive energy per bond of the specific z-coordinated atoms, which satisfies:[109] $\frac{E_{1s}(z) - E_{1s}(0)}{E_{1s}(12) - E_{1s}(0)} = \frac{E_z}{E_b} = C_z^{-2.56}$.

relaxation through external stimulus such as changing coordination environment, temperature or pressure.[94,108]

2.2 Nonbonding electrons polarization

2.2.1 Impurity midgap states. It is emphasized that the E_G derived from the band theory is intrinsic for ideal crystals without involvement of the nonbonding or antibonding interactions. The interaction through regular bonds dictates the framework of band structures.[89] The nonbonding lone pair states generated by the sp³ hybridization of oxygen and nitrogen and the nonbonding unpaired π-states in the sp²-hybridized carbon contribute insignificantly to the band framework because the interatomic interactions through such nonbonding or antibonding states are extremely weak, with energy around 10^{-2} eV.[108] These nonbonding electrons will form however mid-gap impurity states[110] as the nonbonding electrons neither raise nor lower the energies of the initial *p* orbit of the isolated O, N and C atoms.[111] On the other hand, the nonbonding lone pairs will polarize atoms nearby, forming dipoles with electronic states above the Fermi energy. The unpaired σ dangling bond electrons of carbon can be polarized by the nearby electrons and the extent of polarization depends on the density of the latter. This polarization will raise the energy of the unpaired nonbonding electrons, forming the Dirac-Fermi polarons.[112] Extrinsic factors such as the number and the total energy of the electron-hole pairs (excitons) contribute neither to the Hamiltonian nor to the entire band structure.

Upon sp² orbits hybridization, electrons of each carbon atom in the LGS form three σ bonds to the neighboring atoms in a C_{3v} symmetry and the unpaired nonbonding electron of the carbon develops into the π and π* states at the corner of the Brillouin zone or below the Dirac point[113] in the midgap region. Generally, the unpaired π-bond electrons are responsible for both the conductivity and the weak interactions between the layers of graphite. The involvement of nonbonding π-bond electrons distinguishes graphite from diamond in performance—graphite is a conductor yet diamond is an insulator though the covalent bond in graphite is shorter (0.142 nm) and stronger (vibration wave number of 1553 cm^{-1}) than those of diamond (0.154 nm, 1331 cm^{-1}). However, edge creation derives the additional σ dangling bond electrons that are responsible for the Dirac-Fermi edge states.[114]

Charge transition from the mid-gap impurity or the nonbonding states to the upper band edge gives rise to the apparent E_G that is entirely different from the intrinsic E_G calculated under ideal conditions. Unfortunately, the presence and polarization of the nonbonding states are hardly described from the self-consistent optimization in DFT or tight-binding approximations at the present because of the limitation of interatomic potentials. Broken-bond-induced local strain and quantum entrapment at edge that is sometimes several folds deeper than the potential at the usual atomic site in the bulk need to be considered. Potentials suitable for the weak interaction between the nonbonding and the polarized antibonding states are highly desirable for computations.

2.2.2 Edge discriminative Dirac-Fermi polarons generation. At sites surrounding atomic vacancies or at the terminating end

of a solid, the characteristics of the nonbonding lone-electron states become even more pronounced. Polarization occurs to the lone electrons, if existing, by the densely, deeply, and locally entrapped bonding and core electrons of the undercoordinated atoms, as illustrated in Fig. 4.

The following phenomena are expected to happen due to the coupling of the local bond relaxation, quantum entrapment, and lone electron polarization:

(i) The locally locked lone-electron dipoles will form at sites surrounding atomic vacancies, defects, adatoms, GNR edges, atomic chain ends, terrace edges, *etc.*

(ii) The dipole states are readily probed as the Dirac-Fermi polarons using STM/S as high protrusions with energies at E_F.

(iii) The polarized lone electrons demonstrate non-zero spin values being responsible for the measured magnetism in the
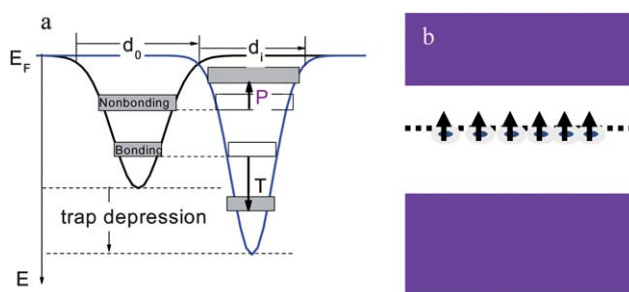

Fig. 4 (a) Atomic-undercoordination-induced local bond contraction ($d_i < d_0$), the associated quantum entrapment (T) and, the polarization of the nonbonding states (P) by the densely, deeply and locally entrapped bonding and core charges.[89] The locally polarized unpaired electrons add impurity states in the midgap region demonstrating non-zero spin each.[115] These processes modulate the Hamiltonian by crystal potential screening and splitting, which determine the charge distribution in the full span of energy.[114]
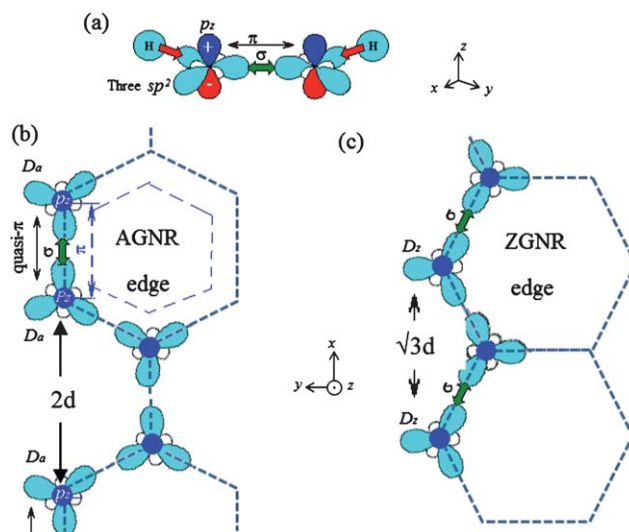

Fig. 5 Schematic illustration of (a) the orbital of graphene atoms with H terminated edge; (b) the "pseudo-π-bond" formation between the nearest (d) dangling σ-bonds for the AGNR and rec-ZGNR edges, and (c) the uniform distance ($\sqrt{3}d$) between the dangling σ-bonds at the ZGNR edge seems too large to allow the "pseudo-π-bond" formation. D_a and D_z represent the AGNR and ZGNR edge states.

graphene edge,[45] graphite atomic vacancy,[40] monolayer terrace edge[41] or graphene ribbon edge[116] terrace edge and nonmagnetic metal clusters,[117] but their stability and intensity are subject to confirmation for practical device applications.

(iv) Due to the potential screening and splitting, the core band may create two extra DOS components at both ends of the core bands. One is the trapped and the other the screened states.[114]

Fig. 5 shows that the GNRs can be categorized in two groups according to the distance between the dangling σ-bond along the edges. The ZGNR and vacancy edges are grouped as I; the AGNR and rec-ZGNR edges as II. The identical but longer atomic distance ($\sqrt{3}d$) at the ZGNR edge and surrounding an atomic vacancy retain the dangling sp^2 orbital nature. Thus, group-I dangling σ bond states are more significant with the Dirac-Fermi polarons generation as a consequence. However, the alternative distances (d and 2d) between the dangling σ-bond along the edge in group II may enable the pseudo-π-bond formation, which reduces the impurity mid-gap states, demonstrating the semiconducting nature.

III C–C bond dimension and strength

- *The elastic modulus is proportional to the binding energy density (E_z/d_z^3) while the melting point to the atomic cohesive energy (zE_z), which causes the paradox in observations compared to bulk specimens.*
- *With the experimentally determined stiffness of 0.368 TPa·nm and the tip-end melting point of 1593 K, the C–C bond in the SWCNT is determined to be ~0.142 nm thick and ~0.125 nm long with a 68% magnitude rise in binding energy, the edge C–C bond is 0.108 nm long and 152% times stronger, in comparison to the bulk diamond values.*
- *The Young's modulus of SWNT is asserted to be 2.60 TPa, 2.5 times the bulk value of 1.02 TPa.*
- *The Young's modulus of MWCNT is proportional to the inverse number of walls and varies insignificantly with the MWCNT radius because the dominance of the outermost walls.*

3.1 Elasticity, chemical and thermal stability

Determination of the Young's modulus (Y) of CNT and GNR has been a confusing issue for a long time; the Y value for the SWCNT has been reported to vary over a range of 0.5–5.5 TPa compared with that of the bulk graphite and diamond (1.02 TPa) irrespective of the single-wall (C–C bond) thickness (t).[64–71] If one assumes the equilibrium interlayer spacing of the graphite sheet, t = 0.34 nm, to represent the wall thickness, the derived Y is ~1.1 TPa.[72,118] If t = 0.066 nm, which is close to the radius of a free C atom (0.0771~0.0914 nm), the Y is derived to be 5.5 TPa.[71] The apparent thickness may change slightly due to the thermal vibration,[119] which should be limited to 5% or lower of the bond length at the temperature of melting.[100] Although the wall thickness and the scattered Y-values need to be certain, the product of Yt was found surprisingly approach to a constant value of 0.368 ± 0.005 TPa·nm.[95]

For the SWCNTs, under the presumed t values, the Y values vary slightly with the tube diameter and the tube chirality because of the curvature-induced strain.[120] However, for the multi-walled (MW) CNTs, two typical trends of the change in Y have been observed:

(i) The Y is almost independent of the tube diameters,[72] and,

(ii) The Y increases as the number of the wall is reduced.[73]

Lee *et al.*[121] measured the elastic properties and intrinsic breaking strength of a free-standing monolayer graphene membrane by nanoindentation in an atomic force microscope (AFM) and found that the force-displacement behavior is nonlinearly elastic, and yields second- and third-order elastic stiffness of 340 Newton per meter (Nm^{-1} = TPa·nm) and −690 Nm^{-1}, respectively. The breaking strength is 42 Nm^{-1} and represents the intrinsic strength of a defect-free GNR sheet. These quantities correspond to a Young's modulus of Y = 1.0 TPa, a third-order elastic stiffness of D = −2.0 TPa, compared with the intrinsic strength of σ_{int} = 130 GPa for bulk graphite. These experiments established graphene as the strongest material ever measured, and showed that atomically perfect nanoscale materials can be mechanically tested to deformations well beyond the linear regime.[122] With a transmission electron aberration-corrected microscope capable of simultaneous atomic spatial resolution and one-second temporal resolution, Girit *et al.*[46] observed *in situ* the dynamics of carbon atoms at the edge of a hole in a suspended, single atomic layer of graphene. The rearrangement of bonds and beam-induced ejection of carbon atoms are recorded as the hole grows. They demonstrated the edge reconstruction and the stability of the "zigzag" edge configuration, revealing the complex behavior of atoms preferentially occurring at the edge boundary. Most strikingly, they discovered that breaking a C–C bond of a 3-coordinated carbon atom in the graphene requires a minimal energy of 5.67 eV per bond and breaking the C–C bond of a 2-coordinated carbon near atomic vacancy needs 7.50 eV per bond; the latter is 7.50/5.67 = 1.32 times that of the former. DFT computations revealed that at room temperature, the ZGNR edge adatom is much more mobile than the atomic vacancy.[123] The findings evidence that the BOLS expectation of atomic undercoordination induced bond strengthening associated with cohesive energy loss due to z reduction.

In contrast, atoms at the tip-end of a SWCNT could melt or coalesce first and then the tube body follows at temperature much lower than the melting point of the bulk diamond ($T_m(12)$ = 3800 K). It has been found that the coalescence of a SWCNT happens at 1073 K under the energetic (1.25 MeV) electron beam irradiation. The coalescence starts at vacancies *via* a zipper-like mechanism,[124] agreeing with that happening to the graphene atomic vacancy.[46] The STM tip-end that is made of CNT starts to melt at 1593 K in ultrahigh vacuum.[74] Annealing at 1670–1770 K under medium-high vacuum, in flowing Ar and N$_2$ atmospheres, 60% of the SWCNTs coalesce with their neighbors.[75] Heating under Ar gas flow in the temperature range of 1873–2273 K results in a progressive destruction of the SWCNT bundle, followed by the coalescence of the entire bundle.[125] SWCNTs transform at temperatures of 2473 K or higher to MWCNTs with external diameter of several nanometres, and the Fe–C impurity bonds can be completely removed at 2523 K.[126] An ordinary camera flash[76] could burn the SWCNT at the ambient conditions, showing the higher chemical reactivity for oxidation of the SWCNT. These results consistently show the lower thermal and chemical stability of the CNT. In particular,

the tip-end of the SWCNTs melts first and then is followed by the wall of the SWCNT. MWCNTs are more thermally stable than the SWCNTs, and the stability of the MWCNTs increases with the number of walls (λ).[64,127,128]

The mechanisms behind the paradox of Y enhancement and the T_m suppression of the CNTs and the certainty in the wall thickness of the SWCNTs are still puzzles, although the atoms that surround defects or are located at the tip ends or at the GNR edges are expected to play unusual, yet unclear, roles in dominating the mechanical and thermal behavior of the CNTs.[129] With the known identities and their functional dependence on the atomic coordination, the dimension and strength of a single C–C bond can be uniquely determined by solving a group of equations, to advance a consistent understanding of the mechanical strength and the chemical and thermal stability of the CNTs, which also applies to the GNRs.

3.2 Formulations

As mentioned, the striking difference between the bulk diamond and a SWCNT is that the effective atomic CN of a C atom reduces from a bulk value of 12 to 3 and the sp orbits hybridization transits from the sp^3 to the sp^2 type upon SWCNT or GNR formation. For an atom near to the defect vacancy or at the open edge of a CNT or a GNR, the CN is 2. One of the sp^2 σ-bond becomes dangling with generation of an unpaired electron in addition to the unpaired π-bond electrons.

With the specified atomic CN for diamond, graphite, and the CNT edges, we can readily determine the shortened bond-length (d_z), the enhanced bond-energy (E_z), and the cohesive energy ($E_{coh} = zE_z$) of a single atom of concern as well as the binding energy density ($E_d = n_z E_z$) in a specific atomic site. The value n_i is the bond number per unit volume. Since the E_{coh} defines the thermal stability,[98] and E_d the mechanical strength,[130] the functional dependence of Y(z) and T_m(z) on the atomic CN and the bond energy at the equilibrium atomic separation are given as:

$$\begin{cases} Y(z) \propto n_z E_z = d_z^{-2} E_z \\ T_m(z) \propto E_{coh}(z) = z E_z \end{cases} \quad (8)$$

For a SWCNT or a monolayer GNR, $n_z \propto d_z^{-2}$ is the bond number per unit area, which is independent of the wall thickness. Obviously, no other argument could change the Y value unless the bond length was shortened and/or the bond energy was increased. At the melting point, the bonds between the under-coordinated atoms will be thermally loosened and the under-coordinated atoms will coalesce with their neighbors.

3.3 CN-dependence of C–C bond length

From Table 1 we can find the BOLS predicted bond strain in comparison to the evaluated values for C allotropes.[95] On the other hand, the C–C bond was suggested to contract varying from 11.2 to 39.8% in the first interlayer spacing of diamond, according to molecular dynamics computations.[131] The mechanical transverse deformation of single layer and bilayer graphene under central loading using a mixed atomistic continuum - Finite Element technique suggested that the C–C bond length is within the range of 0.111 and 0.116 nm for the bilayer,[132] and 0.10 nm for the single layer,[133] agreeing with the

BOLS expectation. The DFT optimized C–C bond lengths[19] follow the BOLS predicted trend but the extent deviates significantly at smaller CN values. The effect of the deviation is enormous as all the quantities discussed herewith depend on the extent of bond contraction.

3.4 SWCNT C–C bond energy and elasticity

Correlation between the measured stiffness $(Yt)_{z=3}$ (0.368 TPa·nm) and the melting point $T_m(z = 2)$ (1593 K) for a SWCNT with the corresponding values for bulk diamond ($T_m(12) = 3800$ K, $Y(12) = 1.02$ TPa) satisfy the relations:[95]

$$\begin{cases} \dfrac{T_m(2)}{T_m(12)} = \dfrac{1593}{3800} = \dfrac{2}{12}c(2)^{-m} = \dfrac{0.6973^{-m}}{6} & \text{(tip-bulk)} \\[2mm] \dfrac{T_m(2)}{T_m(3)} = \dfrac{1593}{T_m(3)} = \dfrac{2}{3}\left(\dfrac{c(2)}{c(3)}\right)^{-m} = \dfrac{2 \times 0.8559^{-m}}{3} & \text{(wall-tip)} \\[2mm] \dfrac{(Y \cdot t)_{z=3}}{Y(12)t_{z=3}} = \dfrac{0.368}{1.02 t_{z=3}} = c(3)^{-(2+m)} = 0.8147^{-(2+m)} & \text{(CNT-wall)} \end{cases}$$
$$(9)$$

This set of equations defines the three unknown quantities of $m = 2.5585 \cong 2.56$, $t_{z=3} = 0.142$ nm and the tube-wall melting point, $T_m(3) = 1605$ K, as listed in Table 2. It is seen that the bond energy enhancement for the 2- and 3-coordinated carbon is 2.52 and 1.69 times (2.52/1.69 = 1.49) the bulk values, respectively, being comparable to the experimental value[46] of 7.5/5.67 = 1.32 with a 10% error tolerance. Furthermore, the activation energy for chemical reaction is also proportional to the atomic cohesive energy. Therefore, the chemical stability of the under-coordinated atoms is lower than the atoms in the bulk, which

Table 1 Comparison of BOLS predicted with the measured and the DFT calculated CN dependence of C–C bond train. z = 2, 3, 4, and 5.335 correspond to the atomic CN of graphene/CNT edge, graphene interior, diamond surface and bulk graphite, respectively. The BOLS prediction has been confirmed by decoding the thermal stability and elasticity of SWCNT[95] and the C 1s core-level shift of carbon allotropes.[109]

Atomic CN	2	3	4	5.335
BOLS[109]	−0.3027[95]	−0.1853[95]	−0.1243	−0.0779[134]
Experimental		-(0.091–0.058)[135]	-(0.112– 0.398)[131]	
DFT[19]	−0.1649	−0.1104	−0.0926	−0.0758

Table 2 With the measured $Yt_{z=3}$ and $T_m(2)$ data as input, solving eqn (9) derived the unique solutions to the C–C bond length, bond thickness, bond energy, the m values, the elastic modulus and the wall interior melting point, which in turn verifies that the quoted data represent true values

$(Yt)_{z=3}$	**0.368** TPa·nm
Tip-end $T_m(2)$	**1593 K**
m	2.5585
Tube wall $T_m(3)$	1605 K
Elastic modulus Y	2.595 TPa
CNT effective thickness t(3)	0.142 nm
Bond length d(2) (c(2) = 0.6973)	0.107 nm
Bond length d(3) (c(3) = 0.8147)	0.126 nm
Bond energy enhancement, E(2)/E(12)	2.52
Bond energy enhancement, E(3)/E(12)	1.69

may explain why the CNT could burn using an ordinary camera flash under ambient conditions. The conclusion is that the CN dependence of C–C bonding identities applies to GNR as well if the curvature effect is weak.

The accuracy of the numerical solutions is subject to the initial input of the measured $T_m(2)$ and $Yt_{z=3}$ values. Errors in measurement or due to structural defects of the CNT may affect the accuracy of the solutions but they never alter the nature of the observations. However, in the current iteration, any variation of the input parameters leads to solutions that are physically forbidden.[95] Therefore, the solution with the quoted $Yt_{z=3}$ and $T_m(2)$ values is unique and, hence, the quoted $Yt_{z=3}$ and $T_m(2)$ values are essentially true for the SWCNT.

3.5 MWCNT elasticity: wall thickness dependence

For the hollow or solid nanobeams (nanorods and MWCNTs), the relative change of a measurable quantity (denoted as Q), which is dependent on shape and size, of a nano-system with dimension K can be quantized with the core-shell configuration as:[95]

$$
\begin{cases}
\dfrac{\Delta Q(K)}{Q(\infty)} = \displaystyle\sum_{i \leq 3} \gamma_i \dfrac{\Delta q_i(d_i, z_i, E_i)}{q(d, z_b, E_b)} \\[2ex]
\gamma_i = \dfrac{\displaystyle\int_{K-i}^{K} x\,dx + \int_{K-\lambda}^{K-\lambda+i} x\,dx}{\displaystyle\int_{K-\lambda}^{K} x\,dx} = \dfrac{i\{(2K-i) + [2(K-\lambda)+i]\}}{\lambda(2K-\lambda)} \\[2ex]
\quad = \dfrac{2(2K-\lambda)i}{\lambda(2K-\lambda)} \propto \dfrac{1}{\lambda}
\end{cases}
$$

$$(10)$$

with q_i being the density of quantity, Q, on an atomic scale is functionally dependent on the bond length d_i, the effective z_i, and the bond energy E_i. The difference of Δq_i between the surface region and the bulk originates the change of the value Q; the surface-to-volume ratio, γ_i, of a nanosolid dominates the trends of Q change. The index value i is counted from the vacuum sides inwards up to a value of 3, because no CN-imperfection is expected for i > 3. The weighting factor, γ_i is the volume ratio of the ith atomic layer to the entire NT with an outer radius K and wall thickness of λ for MWCNT. The ratio $\gamma_S = \sum_{i \leq 3} \gamma_i$ decreases in an inverse fashion (λ^{-1}) from unity to being infinitely small, when the λ grows from unity to infinity. Therefore, it is not surprising that, for a solid rod or a MWCNT with K and λ, the overall $\Delta Q(K)/Q(\infty)$ varies with the inverse radius (1/K) and the $\Delta Q(K)/Q(\infty)$ value differs from the corresponding bulk value ($\Delta Q(\infty)/Q(\infty) = 0$). For a hollow MWCNT of λ thick, the $\Delta Q(K)/Q(\infty)$ should not vary with the diameter of the MWCNT.

These predictions agree with the observed trends in the Y enhancement and the T_m suppression of the nanobeams. The direct evidence for the λ dependence is that the Y value was calculated to vary over a range of 4.7–1.04 TPa when the wall number λ increases from unity to infinity. AFM measurements[118] of the K dependence of the Young's modulus of SiC nanorods and MWCNTs revealed that the MWCNTs are about twice as stiff as the SiC nanorods and that the strengths of the SiC nanorods are substantially greater than those found for large SiC

structures (600 GPa). The Young's modulus is 610 and 660 GPa for SiC rods of 23.0 and 21.5 nm, respectively. For MWCNTs, the modulus is 1.28 ± 0.59 TPa without apparent dependence on the diameter of the nanotubes. The broad range of measured values should be more attributable to the scattered number of walls of the nanotubes than to the error in measurement.

3.6 Summary

Thus, the known $Yt_{z=3}$ value and the known temperature of tip-end melting for a SWCNT, and their functional dependence on the bonding identities, have enabled the dimension and energy of a single C–C bond in SWCNT to be uniquely quantified, which, in turn, deepens our insight into the fascinating mechanical and thermal properties of CNTs and GNRs. The C–C bond between the 2-coordinated carbon contracts by 30% with an association of energy rises by 152% while the C–C bond between 3-coordinated atoms contracts by ~18.5% with energy rises by ~69%. The effective thickness of the C–C bond is ~0.142 nm, which is the diameter of a C atom, rather than the c-axis separation (0.34 nm) of graphite or the radius of a free carbon atom (0.066 nm). The melting point of the tube-wall is slightly (~12 K) higher than that of the tube-end. The unique solution clarifies that the quoted values essentially true for a SWCNT of which the Young's modulus is 2.5 times and the melting point is 0.42 times that of bulk diamond. Predictions of the wall thickness dependence agree well with the insofar-observed trends in T_m suppression and Y enhancement of the nanobeams. The findings provide consistent insight into the unusual thermal, chemical and mechanical behaviors of nanobeams, as well as an effective approach toward bonding identities that are beyond the scope of direct measurement.

IV Binding energy and work function

● *The core level shift upon a carbon allotrope formation from that of an isolated C atom is proportional to the C–C bond energy at equilibrium, and hence the effective atomic CN of the allotrope.*
● *The C–C bond length and energy derived from reproducing the Y and T_m of SWCNT allows the quantification of the C1s binding energies of carbon allotropes with different atomic CNs.*
● *The C1s energy shifts positively by values from 1.32 eV for bulk diamond to 3.33 eV for graphene edges with respect to that of 282.57 eV of an isolated C atom.*
● *The z-resolved C1s energy shift is generalized as: $E_{1s}(z) = 282.57 + 1.32 C_z^{-2.56}(eV)$.*
● *The simultaneous work function reduction and C1s shift evidences the coupling of quantum entrapment and polarization due to undercoordination.*

4.1 C 1s core level shift and work function reduction

Kim *et al.*[86] measured the C1s core-level spectrum of graphene flakes deposited on a SiO_2 substrate with three well-resolved components at 285.97, 284.80 and 284.20 eV (see Fig. 6(a–c)). The layer-number dependence of the graphene grown on SiC substrate has also been reported to follow the same trend.[136] The measured data for other allotropes in Table 3 need to be decomposed and the accuracy of the energy shifts is subject to experimental conditions, such as the incident beam energy and
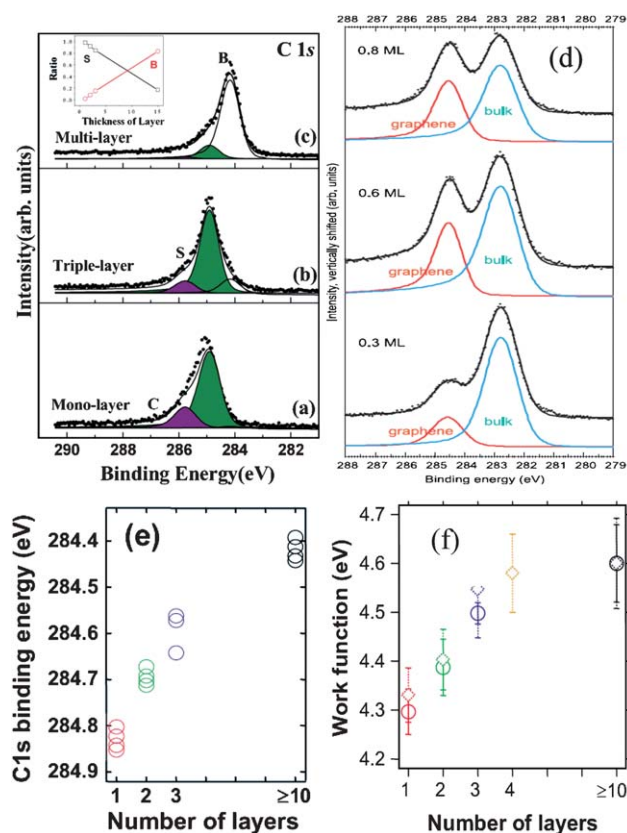
Table 3 Comparison of the BOLS derived with the measured C1s binding energies of carbon allotropes. z = 0 and 12 correspond to an isolated C atom and a C atom in the diamond bulk, respectively. z = 2, 3, 4, and 5.335 correspond to the atomic CN of graphene/CNT edge, graphene interior, diamond surface and bulk graphite, respectively

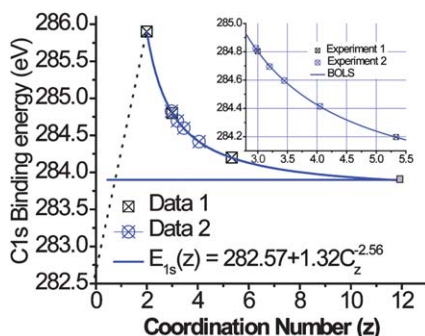| Atomic CN	0	2	3	5.335	12
BOLS derivatives	282. 57	285.89	284.80	284.20	283.89
Measurements	—	285.97[86]	284.80[86]	284.20[86]	283.50–289.30[144–146]
			284.42[141]	284.30[141,142]	
			284.90[142]	284.35[134]	
			284.53–284.74[143]	284.45[135]	

Fig. 7 The BOLS quantified C1s level energies of carbon allotropes. The results are calibrated using the data of graphene ribbons (data 1).[86] Fitting the layer-resolved C1s energy shift (data 2)[87] leads to the correspondence of the effective CN for layer 1(z = 2.97), 2(3.20), 3(3.45) and 10 (4.05), see the inset.

within the broad data range of measurements.[144–146] Exceedingly good agreement between predictions and measurements has thus been realized. Matching the measured layer-resolved C1s level shift[87] has led to the estimation of the effective atomic CN of the few-layer graphene, as can be seen from the inset of Fig. 7. The corresponding effective CNs of the few-layer graphene sheets have been estimated to be 1(z = 2.97), 2(3.2), 3(3.45), and 10(4.05). The graphene sheet size will affect the values slightly.

On the other hand, the work function reduction arises from the elevation of Fermi energy that is proportional to the density of charge centered at a specific energy, E, in the form of $[n(E)]^{2/\tau}$.[147] τ is the dimensionality. Polarization of the nonbonding electrons will raise the density-of-states from lower to higher energies.[90] The observed work function reduction of the few-layer graphene ribbon is in line with the BOLS prediction of the polarization and densification of the nonbonding electrons. Hence, the observed work function reduction and the C1s shift of the few-layer graphene sheets and the graphene flakes can thus be reconciled using the BOLS theory. Agreement between predictions and observations evidences further that the core-level shift results from the broken-bond-induced charge and energy quantum entrapment and the work function reduction arises from the polarization of the nonbonding electrons by the entrapped core and bonding charges. The understanding provides foundation for the Dirac-Fermi polarons generation as demonstrated in section V.

4.4 Summary

Incorporating the BOLS correlation mechanism and the derived bond length and bond energy from the measured elastic enhancement and thermal stability depression with the

photoelectron emission data of the carbon allotropes, we have been able to derive information about the CN-resolved C1s binding energy with a consistent understanding of their physical origin. It is further confirmed that the C–C bond contracts by up to 30% with respect to the bulk-diamond value of 0.154 nm and the C1s binding energy shifts by up to 3.33 eV for graphene edge with respect to the C1s energy of 282.57 ± 0.01 eV for an isolated carbon atom. Reproduction of the observations of the C 1s energy shift and the work function change of the under-coordinated carbon allotropes indicates the dominance of broken-bond-induced local strain and quantum entrapment and the polarization of the unpaired nonbonding electrons by the densely and deeply entrapped core and bonding electrons.

V Dirac-Fermi polarons purification

• *The photoelectron residual spectroscopy (PRS) enabled the atomic scale, zone selective purification of bond and electronic information from selected sites surrounding what a STM/S can scope.*

• *The PRS revealed one extra C 1s component from graphite surface as the consequence of surface entrapment and two at the vacancies as the consequence and origin of the graphitic Dirac-Fermi polarons.*

• *The Dirac-Fermi polarons are clarified as polarization of the dangling-bond electrons by the densely, deeply, and locally entrapped core and bonding electrons that generate the extra states at the bottom of the core band.*

• *The Dirac-Fermi polarons in turn screen and split the crystal potential and hence create an extra component at the top of the core band.*

5.1 STM/S: Dirac-Fermi polarons

STM/S measurements have uncovered the Dirac-Fermi polarons as extraordinarily high protrusions and sharp resonant peak at E_F from sites surrounding atomic vacancies,[40] the edges of monolayer graphite terrace[41,42] and graphene nanoribbons,[43–46] as shown in Fig. 8. When the STM tip moves towards the edge, the extent of polarization becomes more pronounced and the Dirac peak moves nearer to E_F.[43,148] Such features can be resolved neither at the clean graphite surface nor in the GNR interior. The same type of protrusion and Fermi states has also been observed from CNT point defects.[148] The interlayer interaction was suggested to play a crucial role in deriving the STM protrusions and the sharp STS features.[149] One may note that the Dirac-Fermi polarons generated at surface atomic vacancy and at the ZGNR edge are naturally the same despite the spectral sharpness. This fact allows us to investigate the origin of the
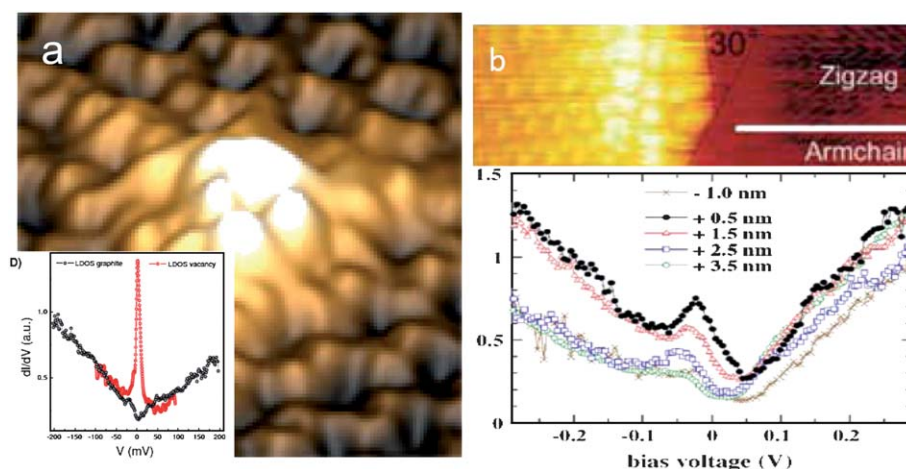
Fig. 8 STM images of (a) graphite surface vacancy[40] and (b) the ZGNR edges[45] showing the Dirac-Fermi polarons with high protrusions and the spectral resonant peaks. The Dirac fermions at vacancy and GNR edge are morphologically and energetically identical despite the spectral sharpness. This fact allows us to focus on the fermions generated at graphite surface vacancies instead of the ZGNR edges using XPS.

polarons by focusing on the vacancy defect at graphite surface using XPS because the weak signal of the GNR sheets.

However, the physical origin and the driving force for the generation and retention of the Dirac-Fermi polarons remain unclear. Zhang *et al.*[150] observed the fluctuations in graphene charge density and attributed them to charge-donating impurities below the graphene. These impurities induce standing wave patterns due to unexpected backscattering of Dirac fermions. In order to identify the nature of the Dirac-Fermi polarons, information regarding the behavior of the surrounding bonds and the energetically low-lying electrons as the "roots" is highly desired. Unfortunately, such localized information is as yet by no means available. A method of photoelectron residual spectroscopic (PRS) purification for this purpose has thus been developed, which has enabled the fermions to be correlated with their neighboring bonds and the performance of the low-lying electrons. Findings confirm that the defect fermions result from the polarization of the dangling-bond electrons by the under-coordination-induced local quantum entrapment and densification of the energetically low-lying electrons.

5.2 PRS purification

Using an STM/S, one can easily image an individual atom by probing the flow of charge with energies in the vicinity of Fermi level under bias across the tip and the sample surface. Information obtained as such is limited only to the top edge of the valence band in energy and to the open side of the surface atoms in real space. In comparison, an XPS collects statistical and volumetric information of electrons and bonding interaction up to several nanometres in depth[151] with energies in the valence band and below. From the conventional approach of XPS data decomposition, one is hardly able to gain information of the contribution from the subsurface before and after physical and chemical conditioning as the signal due to such modification is rather weak. Besides, uncertainty remains regarding the number and the relative energies of the XPS spectral components. Furthermore, the direction and the reference point for the core

level shift need to be certain. It has been consistently confirmed[105–107,152] that the undercoordination induces positive shifts from the energy levels of an isolated atom. The missing link between STM/S and XPS is how to combine the atomic-scale STM/S and the volumetric statistical XPS to gain the atomic scale, zone selective bond and electronic information from zones surrounding undercoordinated atoms, from which the STM/S can hardly scope.

One can imagine what will happen in the following processes. Upon the spectral background correction and area normalization, the difference between two spectra collected: (i) from the same defect-free surface at different emission angles and (ii) from the same surface after and before conditioning under the same experimental conditions. The residual spectrum (i) keeps only the extra features due to the skin up to two atomic spacings and filters out the bulk information as the XPS collects more information from the surface at larger emission angles[153] and more from the bulk at the smaller angles.[141] Using the same Al K_α source, Speranza and Minati[151] found that the X-ray penetration depth in graphite decreases from 8.7 to 0.7 nm when the emission angle is increased from 0 to 85°. Likewise, the residual spectrum (ii) purifies the features merely due to surface conditioning such as defects generation in the current experiment. This technique can be used for any surface conditioning such as crystal growth, chemical reaction, alloy formation, *etc.* These processes purify the energy states of concern limited to the atomic-scaled zones surrounding the fermions as this process filters out the artifact background and bulk information. Besides the information purification,[151] the additional advantage of the PRS is that it can minimize the influence of extrinsic factors such as the background uncertainty, surface sensitivity, and the "initial-final states" effect existing throughout the course of measurements.

In order to correlate the energetic behavior of electrons detected using STM/S and XPS, we conducted XPS measurements of graphite surface with and without artificial vacancies at room temperature. We firstly collected the XPS data from a graphite surface without vacancy defects at different emission angles (between the surface normal and the emission electron

beam) using the standard XPS (Al K_α sourced at 1486.6 eV) apparatus and standard procedures. The emission angle was varied within the range of 25 and 75°. The highly oriented pyrolytic graphite (HOPG) was cleaved using the adhesive tape in air, and then transferred quickly into the XPS chamber. In order to examine the effect of vacancy generation, the surface was sputtered using Ar^+ ions with 0.5 keV energy and incident along the HOPG surface normal. The spray dose was controlled by the sample current and the duration of sputtering. The energetic Ar^+ sputtering increases only the number of dangling bonds and the density of surface defects in vacuum.[154]

5.3 Edge and surface states: entrapment and polarization

The raw XPS spectra collected from the defect-free surfaces at different emission angles and from the defect surfaces of different doses at 50°, as shown in Fig. 9a and b, are well resolved, exhibiting an attenuated and broadened nature, as reported in the open literature.[141,155,156] However, the overall intensities of the raw spectra are relatively weaker for those collected at larger angles or from roughened surfaces because of the scattering loss. This effect can be compensated by the spectral area normalization under the guideline of spectral area conservation, which means that the area integration of each spectrum, and therefore, the total number of excited electrons in each of the collected spectrum is the same across spectra.

In practice, we firstly corrected the spectral background using the standard Shelly process and then normalized the spectra area. The spectra collected from the defect-free surface at larger emission angles were then subtracted by the referential one collected from the freshly-cleaved surface at the smallest (25°) available angle. For the surfaces with defects, we simply repeat the process at 50° without changing the emission angle.

Fig. 10 compares the evolution of the residual XPS spectra with the emission angles of the defect-free surface and with the surface defect densities as represented by the dose of Ar^+ sputtering at a fixed emission angle of 55°. The spectral areas above and below the energy-axis represent, respectively, the gain and loss of the energy states. The net spectral gain should be zero because of the rule of spectral area conservation. The walleyes centered at 284.1 and 284.4 eV of the residual spectra correspond, respectively, to the bulk and the surface component.

For the defect-free surface, only one trapped peak (T_S) is present at the bottom of the C 1s band, which shifts further to a lower binding energy corresponding to the change of the effective atomic CN from $z \sim 4$ to $z \sim 3.2$, as the emission angle increases from 35° to 75°. The presence of the T_S component
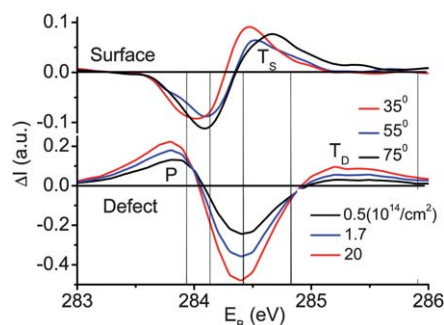
Fig. 10 The PRS of graphite surface shows only the trapped (T_S) surface states evolving from $z \sim 4$ to $z \sim 3.2$ when the emission angle is increased. The vacancy-density-resolved PRS shows both the trapped (T_D) and polarized (P) states and their correlation. The energy separation between the emerging entrapped component and the $E_{1s}(0) = 282.57$ eV satisfies: $E_{1s}(z) - 282.57 = 1.32C_z^{-2.56}(eV)$. The valleys centered at 284.1 ($z = 5.335$) and 284.4 eV ($z = 4$) correspond, respectively, to the removed obvious bulk and surface information and the extra components are the energy states due to the surface skin (T_S) between the outermost two atomic layers and sites surrounding vacancy defects (T_D). The P component at the upper edge arises from the screening and splitting of the crystal potential by the Dirac fermions that originate from the polarization of the entrapped core electrons.

indicates that the bonds between undercoordinated surface atoms are indeed shorter and stronger. The trend of the T_S evolution with the emission angle also indicates that the surface-induced quantum entrapment is more significant when the effective atomic CN is decreased.

As defects are generated, the T_S moves even deeper and evolves into T_D. The T_D is accompanied by the presence of the Dirac-Fermi polarons at the Fermi level[40] and the P component at the upper edge of the C 1s band. As the defect density is increased, the intensity of the T_D component grows and the P component moves up in both energy and intensity. The effective CNs of the defect atoms changes insignificantly if the T_D energy remains unchanged. The presence of the T_S and T_D peaks in both cases verify the BOLS premise of bond contraction and the associated bond strength gain and quantum entrapment. The fact of the T_D energy being lower than the T_S energy indicates that the bonds between the defect atoms are even shorter and stronger than those in the clean surface.

Fig. 11 summarizes our findings of the purified XPS collected at 75° emission angle from surfaces with and without defects. The effective atomic z of the graphite skin is ~ 3.2 and the z for the vacancy neighbors is ~ 2.5. The P states are centered at 283.63 eV, 0.31 eV above that (283.94 eV) of bulk diamond. Therefore, the polarization coefficient $p = (283.63–282.57)/(283.94–282.57) = 1.06/1.32 = 0.80$, which means that the screened potential is 20% shallower than that in diamond, while the vacancy trapping potential is $C_{z=2.5}^{-2.56} - 1 = 0.97$ times deeper. According to the energy band theory,[100] the ratio of the separation between the T_S or the T_D and the $E_{1s}(0)$ is proportional to the respective bond energies. The defect bonds (T_D components) are expected as $C_{z=2.5}^{-2.56}/C_{z=3.2}^{-2.56} = 1.23$ times stronger than the surface bonds (T_S), which agrees with the estimated values of $(285.25–282.57)/(284.70–282.57) = 1.25$. This trend also agrees with the trend (1.32) of energy requirement for the 2- and 3-coordinated graphene bond breaking.[46]
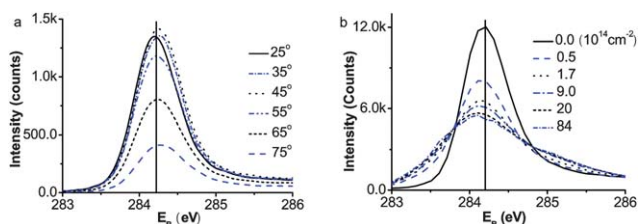

Fig. 9 Raw XPS spectra collected from (a) the vacancy-free HOPG surface at different emission angles and from (b) the defect surface collected at 55° of different Ar^+ spray doses.
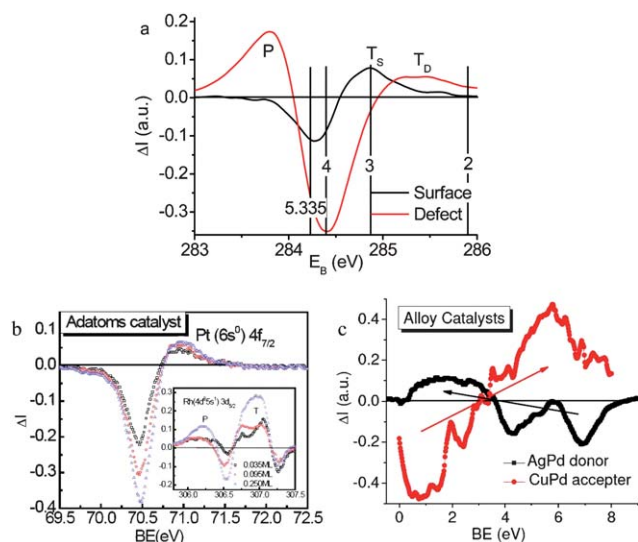
Fig. 11 (a) Comparison of the purified XPS C 1s spectra collected at 75° from the surface with (9×10^{14} cm^{-2} dosed Ar$^+$ spray) and without defects. The P, T_S and T_D indicates the polarons screened, surface ($z \sim 3$) and defect ($z \sim 2.3$) entrapped components; D and G indicate the C 1s energies for the bulk diamond ($z = 12$) and graphite ($z = 5.335$). (b) The purified XPS for the Pt and Rh adatoms[152] and (c) the valence band of CuPd and AgPd alloys[157] showing the spectral similarity of C vacancy to that of Rh adatoms and AgPd alloy and the similarity of graphite surface to that of Pt adatoms and CuPd alloy. Pt and CuPd have been identified as acceptor-type and the Rh and AgPd donor type catalysts.

With the obtained values of z = 3.2 for surface and 2.5 for defects, one can estimate the local bond length (C_z), bond energy ($C_z^{-2.56}$), atomic cohesive energy ($zC_z^{-2.56}/12$), and charge density (C_z^{-3}) localized in the respective zones.

It is encouraging to note that from the comparison of the purified core band to those in Fig. 11 obtained from the well-defined catalysts of Pt and Rh adatoms[152] and CuPd and AgPd alloys,[157] graphite flat surface may serve as an acceptor-type while the defect surface as donor-type catalyst because of the respective polarization and entrapment. The former is more beneficial to hydrogenation and the latter oxidation. One of the key identities of a catalyst is the capability and direction of charge flow between the catalysts and the reactant such as CO and ON gaseous specimens.
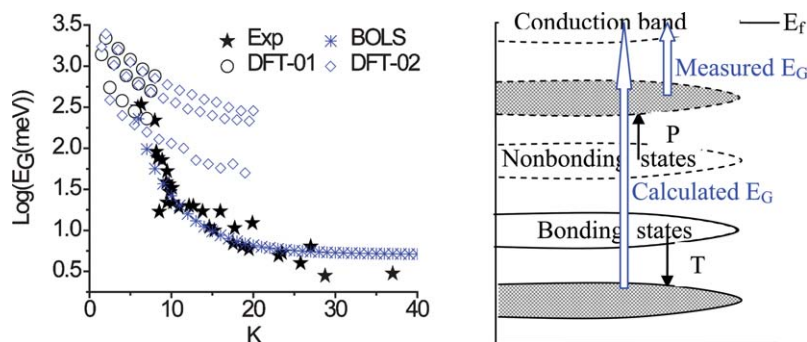
5.4 Summary

The findings verify the theory predictions and clarify the origin of the defect charge polarization observed using STM/S and their correlation with the PRS C1s band P and T states. It becomes clear that: (i) the shorter and stronger bonds between under-coordinated atoms cause local quantum entrapment of charge and energy that produces the trapped component in the core band; (ii) the densely, deeply, and locally entrapped core charge polarizes the unpaired dangling-bond electrons to produce the Dirac-Fermi polarons; (iii) and the Dirac polarons in turn screen and split the potential and then generate the polarized component in the core band. STM/S and PRS are correlated and complement each other. The former collects the polarized states near E_F and images the surface dipoles as protrusions at the atomic scale;[108] the latter collects statistic information regarding the entrapped T and the screened P states from zones right aside that STM/S scoped. Complementing the STM/S, the PRS is therefore much more revealing than using XPS or STM/S alone in gaining bond and electron information at the atomic scale, selected zones of surface, subsurface, defects and impurities as well. A comparison with the spectral features of Pt and Rh adatoms, AgPd and CuPd alloys suggests that the graphite surface with and without defect may serve, respectively, donor- and acceptor-type catalysts because of the respective dominance of polarization and entrapment.

VI GNR band gap expansion

- *A perturbation in the Hamiltonian by the edge strain and quantum entrapment dictates the band structure change.*
- *The presence and polarization of the dangling-bond states mediates the measured gap, resulting in discrepancy between theory calculations and experimental observations.*
- *Edge H-termination minimizes the midgap impurity states without significant influence on the band gap width.*

6.1 Width dependence inconsistency

The E_G of the AGNR has been found roughly proportional to the inverse width of the GNRs.[48,60–62] Electron transport dynamics measurement[61] at temperatures below 200 K revealed that the E_G varies with the GNR width W in a way of: $E_G = \alpha/(W - W_0)$, with the values of $\alpha = 0.2$ eV nm and $W_0 = 16$ nm. When

Fig. 12 Discrepancy between the DFT calculated[48] and the conductance-measured[61] E_G expansion of GNRs (left). Numerical fit based on BOLS consideration can be realized by employing a width dependence of non-constant m values.[19] The DFT describes more intrinsic E_G under ideal conditions while the experimental presents more on the apparent E_G mediated by the mid-gap impurity states (right).

the GNR is narrower than W_0, the E_G increases abruptly to several eV and then approaches the values derived from DFT calculations.[19,48] The E_G in the electrically gated bilayer graphene can be tunable up to 250 meV.[158] Fig. 12 compares the DFT calculated[48] and the measured[61] width dependence of E_G expansion. Calculations suggested that the E_G of the AGNR expand from some 0.25 to 2.5 eV when the K is decreased from 20 to 1.5 with the feature of 3n periodicity. However, the conductance measurements revealed that the apparent E_G increases from several meV to 2.0 eV when the width of the GNR is decreased from K = 40 to K = 5. The measured data shows neither the DFT-derived 3n oscillation nor orientation dependence. This inconsistency indicates clearly that the measurements in real situations and the calculations under ideal conditions are dominated by different mechanisms.

Despite the magnitude difference between the measurements[61] and the theoretical calculations,[48,62,78] the energetic origin for the width-dependent E_G expansion is under debate. The E_G expansion is attributed to the carrier confinement,[48,81,96,159] edge distortion,[60] edge energy pinning,[62,81,160] doping,[79] defects forming,[80] symmetry breaking,[82] substrate interaction,[83] and quantum confinement.[45] By introducing a phenomenological hopping parameter t_1 for the nearest-neighbor hopping integral to represent various chemical edge modifications, in the tight-binding calculations, Wang et al.[81] found that if the t_1 is identical to that in the ribbon interior, no significant E_G expansion occurs. Therefore, the E_G expansion originates from the hopping integral t_1 at edge should certainly be greater than those in the GNR interior.[81,159] A relaxation of the edge structure of AGNR is crucial to obtaining a non-metallic band-gap.[161] Conductance calculations suggested that edge disorder[162] in AGNRs could cause short localization lengths which could make expected semiconducting GNR devices insulating. A single edge defect could even induce localized states and consequently zero-conductance dips.[163] The edge and defect states are therefore critical to the performance of GNRs[60] in addition to the edge chemical passivation by boron,[164] nitrogen,[165] oxygen,[166] or fluorine.[167] When the spin polarization is considered, both symmetric and asymmetric ZGNRs present semiconductor behavior, which is different from spin-unpolarized result showing metallic nature.[168] Transition between semiconductor and metal can be induced by the combination of both radial and elongation deformation.[169] The bandgap and conductance can also be modulated by folding the graphene.[170] These addends not only change the band structures of the AGNRs but even result in observable metal-to-insulator transition.

It is unexpected that the BOLS, the DFT, and the experimentally measured results are inconsistent.[19] Although we have reproduced the size dependence of the thermal stability, mechanical strength, band gap and core-level shift of numerous specimens including the SWCNT and the nanostructured silicon,[90] the BOLS appears uncertain to reproduce the width trends of the E_G for GNRs. The inconsistency indicates however the impact of the nonbonding mid-gap states and the inhomogeneous stress caused by edge chemisorption, which can hardly be represented at the present in theoretical computations. The nonbonding states dominate the apparent E_G as one can measure the transition of electrons from the mid-gap impurity states to the tail of the conduction band rather than from the valence to

the conduction band directly (Fig. 12, right panel).[110] From this perspective, experiments measure the true but not the intrinsic E_G. The measured trend of E_G expansion gives information about the change of the separation between the upper edge of nonbonding states and the conduction band tail, instead.

6.2 DFT: Dispersion of impurity states

It is our opinion that the E_G is determined intrinsically by the crystal potential and hence the Hamiltonian matrix while the density and energy of carriers in GNR play their roles in the transport dynamics. In order to verify the contribution of edge strain and quantum entrapment to the band gap expansion, DFT calculations were performed on various carbon structures with different atomic CNs to gain the valence DOS and C–C bond lengths and the E_G expansion as shown in Fig. 12.[19] As compared in Table 1, the DFT derived extent of C–C bond contraction follows not well the BOLS expectation in particular at the lower CN values though the calculated E_G reproduces the results reported in ref [48]. As such, the calculated charge densification is lower than that expected for the BOLS. By taking the unusual edge strain-and-trap boundary conditions into consideration, i.e., a potential barrier followed immediately by the deep potential trap, quantum calculations may produce the BOLS expected results.

6.3 BOLS-TB: Edge quantum entrapment

Stimulated by the BOLS, DFT, and experimental discrepancy, we developed an edge-modified BOLS-TB approach to examine the E_G expansion of the AGNR(II) and the rec-ZGNR(I)[63] as illustrated in Fig. 13. An atomic vacancy is also shown at the N = 11 point. The t is the overlap integral between two adjacent atoms in the ribbon interior; t_1 and t_2 are the integrals at edges.[96] The BOLS derived strains and overlap integrals are listed in Table 4.
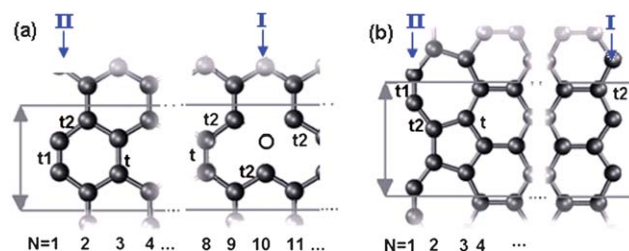
Fig. 13 Atomic structures of (a) the AGNR(II) and (b) the rec-ZGNR(II) edge of infinitely long ribbons with N represent the atomic positions. t is the overlap integral between two adjacent atoms in the ribbon interior; t_1 and t_2 are the integrals at edges.[96] The I indicates the ZGNR edges.

Table 4 The BOLS-TB parameters for calculating the E_G of AGNR and rec-ZGNR. The strain is set with respect to the bond length of diamond according to the z-dependent contraction coefficient.[96]

Bond position	t_1	t_2	H–C edge	Interior	Graphite[109]	Diamond[109]
z	2	2.5	2.125	3	5.335	12
Strain (%)	−30.2	−23.6	−11.5	−18.5	−7.8	0
Integral	1.49t	1.17t	1.11t	t = −2.4 eV		

Fig. 14 compares the band structure of an AGNR-11 obtained using (a) the conventional TB, (b) the BOLS-TB, with the strain and overlap integrals as given in Table 4, and, (c) the DFT calculation results. A high DOS degeneracy at $E = \pm 2.7$ eV in (a) suggests that the system is unstable. This frustration can be avoided by using the modified BOLS-TB and DFT methods. Since there are 22 unpaired p_z electrons in the AGNR-11 unit cell, 22 double-degenerated bands will be present. The Fermi level lies at the middle of the E_G. The E_G opening can be observed in the BOLS-TB (b) and the DFT (c) derivatives. The dangling-bond electrons provide impurity level closing to the Fermi energy, which has no significant effect on E_G.[110,171]

Fig. 15 compares the E_G of both the bare and the H-adsorbed AGNRs as a function of the ribbon width N. The conventional TB results in the zero E_G when $N = 3p + 2$ (p is an integer); while the modified BOLS-TB results in the E_G opening, which is consistent with the reported DFT[48,62] and experimental observations.[61] The edge absorption of H does not affect the E_G generation or the expansion trend significantly. Findings confirm further that the edge strain and quantum entrapment originate the E_G expansion of GNR with and without H-termination and rationalize further Wang and co-worker's findings.[81] The effect of H-passivation on the band gap width is the same as the

hydrogenation of amorphous silicon.[110] The hydrogenation of GNR edges annihilates the dangling bond states and hence minimizes the midgap impurity states without affecting the band gap substantially. Likewise, calculations of the rec-ZGNR with and without H-passivation using these three methods derived the similar results. A very small E_G (~0.1 eV) is generated near the Γ point using the latter two methods.[96]

6.4 Dispersion linearization

As the GNRs C–C bond contracts by up to $C_{z=2} - 1 = 0.3$, the corresponding reciprocal lattice and the Brillouin zone edge will expand by $0.7^{-1}(\sim 1.4)$, the band width also expands by $0.7^{-2.56} = 2.52$. This reciprocal reconfiguration will stretch the dispersion relation $E_\nu(k)$ for the valence band and below with a certain extent of linearization.[19] As we know, the energy dispersion determined by the Hamiltonian determines the effective mass, $\hbar^2[\nabla_k^2 E_\nu(k)]^{-1}$, and the group velocity, $\nabla_k E_\nu(k)/\hbar$, of boding electrons. The stretching and linearization of the dispersion may result in a lowered group velocity, $\nabla_k E_\nu(k)$, and enlarged effective mass of bonding electrons instead, because of the drop of $\nabla_k^2 E_\nu(k)$ with the linearization. The smaller effective mass and the higher group velocity evidence that the Dirac-Fermi polarons located at the corner of the Brillouin zone of the GNRs follow neither the linear dispersion nor occupy the allowed states in the valence band and below, as we expected.

6.5 Summary

The BOLS-TB algorithm has enabled us to clarify the energetic origin of the width dependence of the GNR E_G expansion. The shorter and stronger bonds between the under-coordinated edge atoms and the associated edge quantum entrapment provide the perturbation in the Hamiltonian and initiate the E_G opening with the nonbonding states mediation. The discrepancy between theory and experimental observations has been clarified as the involvement of the nonbonding states. H passivation can remove the midgap nonbonding states while the passivation has no influence on the intrinsic band gap. In the conductance measurements, however, the midgap states contribute to the real E_G. As a consequence of the bond contraction, the Brillouin zone will be stretched and the dispersion will be linearized, which will lower the group velocity and enlarge the effective mass of the bonding electrons, opposite to the trend that the nonbonding states demonstrate.
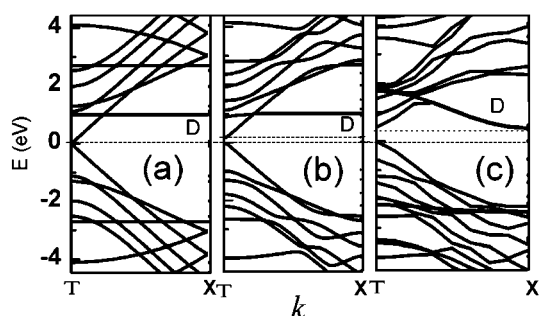

Fig. 14 The band structures of the AGNR-11 calculated using (a) the conventional TB, (b) the BOLS-TB, and (c) the DFT methods. The dangling-bond electrons provide impurity states (broken lines) near the Fermi energy, indicated by D. An E_G is generated in (b) and (c), and the dangling-bond states do not affect the E_G in calculations.[96]
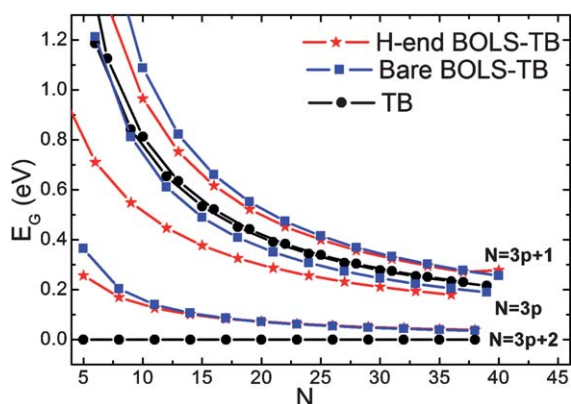

Fig. 15 Comparison of the width dependence of the E_G in bare and H-passivated AGNRs shows absence of E_G expansion for the $N = 3p + 2$ in the conventional TB approach.[96] The BOLS-TB results have the same trend to those of DFT,[48] clarifying the origin of the width trends of E_G expansion. H-termination changes insignificantly the band gap.[110]

VII Magnetism of Dirac-Fermi polarons

● *Difference in the edge atomic distance is uncovered to govern the selective generation of graphitic Dirac-Fermi polarons being weakly anchored dipoles.*

● *The high spin densities of atoms surrounding atomic vacancy or ZGNR edge result from the polarization of the dangling σ-bond by the densely entrapped bonding and core electrons.*

● *The low spin densities of the AGNR and the rec-ZGNR edges originate from the pseudo-π-bonds formation between the nearest dangling σ-bonds along the edges.*

● *H tends to form bond with the polarized dangling sp² electron and to annihilate the DFPs with high-spin-density but hardly to the entrapped dangling p_z electron with low-spin-density. C–H bond*

formation annihilates the Dirac-Fermi polarons and turns the LDOS from the asymmetric dumbbell-shaped sp² dominance to the spherical-shaped p_z dominance.

7.1 Observations

The occurrence of spin polarization of graphene zigzag ribbons was first demonstrated by Fujita *et al.*,[172] and confirmed by subsequent first-principles calculations.[48,173] Without considering the edge strain and quantum entrapment, Fujita *et al.*[172] found that the graphite ribbons show a striking contrast in the electronic states depending on the edge shape in their TB Hubbard model calculations. They showed that even an infinitesimal onsite Coulomb repulsion induces finite magnetization of edge atoms of about 0.2 μ_B. The μ_b is the Bohr magnetron. In particular, a zigzag ribbon shows a remarkably sharp peak of density of states at the Fermi level, which does not originate from infinite graphite. They suggested that the singular electronic states arise from the partly flat bands at the Fermi level, whose wave functions are mainly localized on the zigzag edge. A similar magnetic ground state was found for the ZGNRs without hydrogen termination, but in this case the magnetic moment per atom is much larger, 1.28 μ_B.[174] It has further been confirmed both experimentally and theoretically that the GNR or CNT magnetism is closely related to the structure defects,[175–179] vacancies,[180] edges,[181] and spin polarization of p orbitals,[115] disregarding the magnitude difference.

The magnetic moment was found higher for samples fabricated at 873 K than those fabricated at 673 K; higher temperature fabrication generates higher density of defects.[182] An experimental work revealed that the resolved magnetic edge states originate from the open edges as high-temperature annealing can turn the open edges to loops and hence lowers the magnetic moment.[183] The presence of the unusual magnetism at GNR edge is selective and the magnetic momentum varies with the shape, the density of the vacancies,[180] the hydrogen termination position,[184] and the vacancy sites on the hexagonal sublattice.[185] It has been quite certain that the magnetic moment can be easily detected from the ZGNR edge and the atomic vacancies but hardly from the AGNR edges.[49,59,186] Partially opened CNT also demonstrate magnetic properties.[187] The magnetism of the newly discovered rec-ZGNR edge[63] is to be explored.

Theoretical computations have been extensively conducted with different mechanisms. A TB calculation with the mean-field Hubbard approximation[180] suggested that the conventional Lieb theorem[188] is unable to produce and explain the experimentally observed local magnetism of the GNR vacancy, and hence a model of "charge imbalance" was proposed. A first-principles calculation[185] claimed that the magnetism is determined by the corresponding hexagonal defect sublattice. The defect magnetic moment was lowered from 1.12–1.53 μ_b to 1.0 μ_b upon hydrogenation according to this sublattice model. A DFT calculation[184] showed however that adsorption of H on one of the dangling bonds of a vacancy gives rise to a magnetic moment twice as high as that of a bare vacancy. Using positron annihilation in conjunction with ferromagnetic moment measurements and DFT calculations, Yang *et al.*[189] found that the magnetic moments are closely correlated to the existence of the vacancy defects. The ground state of the vacancy has spin ≈ 1 μ_b, and spin density is localized on the broken bond of carbon.[115] From a systematic calculations using a combination of the mean-field Hubbard model and the first-principles, Yazyev[190] and Singh and Kroll[191] concluded that only single-atom defects can induce ferromagnetism in the GNR-based materials. Volnianska and Boguslawski[115] suggested that the strong spin polarization in the p orbitals as a common denominator for the defect magnetism of solids containing O, N and C. In the case of vacancies, spin polarization is local and results in their high spin states. For a two-dimensional topological insulator, accumulation of spins (momentum) occurs only at edge states, which distinguish topological insulators from conventional ones.[192] Therefore, issues such as the physical origin of the Dirac-Fermi polarons edge selective generation and the effect of hydrogenation remain open to the community.

7.2 BOLS-TB Hubbard spin-polarization

Recently, we proposed that the defect magnetism of solids containing neither transition metals nor rear earth arises from the polarization of nonbonding electrons by the densely, deeply, and locally entrapped bonding and core electrons or by the electron lone pairs of N, O, and F.[89] The nonbonding electrons include the covalent dangling bonds of Si and carbon, electron in the outermost shell of metals. In order to clarify the physical origin of the graphitic magnetic momentum, BOLS-TB and DFT were conducted to verify our proposals of the defect magnetism.[89] The DFT calculations were carried out using the DMOL³ code with a double numeric plus polarization basis set.[193] The geometric and electronic structures of various carbon allotropes were obtained based on the generalized gradient approximation in the Perdew-Burke-Ernzerh form of potential.[194] The calculations were focused on the coordination dependence of C–C bond length, the energy states of various carbon allotropies, and the GNR width dependence of band gap expansion, as given in the previous section.

As far as the π and π* orbitals of the C $2p_z$ electrons are concerned, the BOLS-TB Hamiltonian matrix elements are

$$\begin{cases} \Delta_i = \varepsilon_{2p_z} + <2p_z|V_{cry}(1 + \Delta_z)|2p_z> = \varepsilon_{2p_z} + \alpha & \text{(Diagonal elements)} \\ t_{ij} = <2p_{zi}|V_{cry}(1 + \Delta_z)_i|2p_{zj}> & \text{(Off-diagonal elements)} \end{cases}$$

$$\begin{cases} \dfrac{t_{22}}{t_{33}} = \dfrac{C_2^{-2.56}}{C_3^{-2.56}} = \dfrac{2.52}{1.69} = 1.49 \\ \dfrac{t_{23}}{t_{33}} = \dfrac{C_{2.5}^{-2.56}}{C_3^{-2.56}} = \dfrac{1.97}{1.69} = 1.17 \end{cases} \qquad (14)$$

where V_{cry} is the crystal potential; ε_{2pz} is the eigen core level energy of the $2p_z$ orbital of a carbon atom; α is the onsite exchange integral of negative value; t_{ij} is the overlap hopping integral of the nearest neighbor jth atoms and t_{33} is the interior integral being taken as -2.4 eV. For the H-end edge bond contraction coefficient, C_H, is defined as the bond length ratio between GNR edge and interior, and taken as 96% according to DFT relaxation results.[48] Considering the edge dangling bond, the off-diagonal terms of the Hamiltonian between the dangling bond state and the p_z orbital are zero, because they have different symmetries in the z-direction.[160] Thus, we only consider the diagonal term Δ_D, the dangling bond energy.[96]

Because of the edge strain and quantum entrapment, the α and t_{ij} will be enlarged proportionally to the bond energy by $C(z)^{-m}$. The t_{ij} enhancement has been observed using DFT calculations,[195] as compared in Fig. 16. It is seen that the BOLS expectation and DFT calculation are in good accordance despite the tiny divergence at the shorter end.

The spin texture is determined intrinsically by the Hamiltonian and the charge population in the valence band and above. In particular, the local TB Hamiltonian elements and the charge is non-uniform, which varies from site to site according to the atomic coordination and geometric orientation. The spin-polarized TB Hamiltonian in the mean-field Hubbard model is given as:[196]

$$H_\sigma = \sum_{i,\sigma} \Delta_i c_{i,\sigma}^+ c_{i,\sigma} + \sum_{<i,j>,\sigma} t_{ij}\left(f_{ij} c_{i,\sigma}^+ c_{j,\sigma} + f_{ij}^* c_{j,\sigma}^+ c_{i,\sigma}\right)$$
$$+ \sum_i U_i \hat{n}_{i,\sigma} \hat{n}_{i,-\sigma} \qquad (15)$$

where σ indicates the spin. Δ_i and t_{ij} remain the meaning of eqn (14). The last term is the Hubbard electron repulsion term H_U. Supposing the U_i a constant U, the k-dependent electron repulsion within the mean-field approximation becomes,

$$H_U(k) = U \sum_{i,\sigma}\left[\left(\langle \hat{n}_{i,-\sigma}\rangle - \frac{1}{2}\right) c_{i,\sigma}^+(k) c_{i,\sigma}(k)\right]$$

where

$$\langle \hat{n}_{i,\sigma}\rangle = \frac{1}{2\pi}\int_{-\pi}^{\pi} dk \left\langle c_{i,\sigma}^+(k) c_{i,\sigma}(k)\right\rangle \qquad (16)$$

When the single-site electron repulsion H_U is considered, the numerical calculations can be performed with a self-consistent-field convergence.
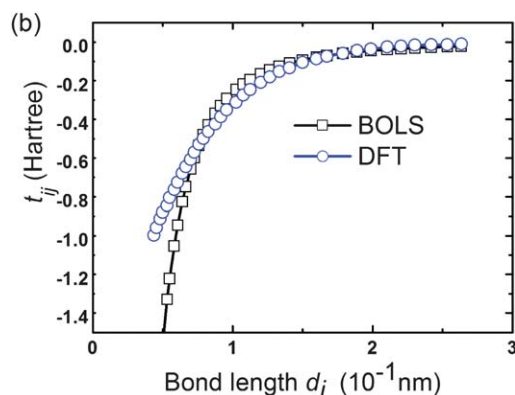

Fig. 16 Correlation between the t_{ij} and the bond length d derived from the DFT results[195] in comparison to the BOLS prediction.

7.3 Energy dispersions and vacancy LDOS

As expected, the DFT energy dispersions in Fig. 17 show that the dangling σ-bond at atomic vacancy (D_v) and ZGNR edge (D_z) show only one sharp state located at Fermi energy. It is therefore confirmed that the Dirac-Fermi polarons correspond to the polarized dangling σ-bond sp^2 electrons, being consistent with PRS observations.[114] However, the dangling σ-bond of the AGNR (D_a) and the rec-ZGNR (D_r) edge behave more like the π and $π^*$ bands with additional two states located far away from the E_F: one is above and the other is below the E_F. This result confirms the expectation of pseudo-π-bond formation of the dangling σ bonds at the AGNR and rec-ZGNR edges. Hence, the BOLS-TB consideration of the Hamiltonian elements for the dangling sp^2 electrons of group II is necessary. As compared, hydrogenation removes these additional impurity states, being exactly the same as observed from hydrogenated silicon.[110]

An examination of the LDOS contour plot exhibiting the midgap Dirac-Fermi polarons localized at the atomic vacancy.[96] In addition to the Dirac fermions, the quantum entrapment and polarization at the vacancy is found more pronounced than those at the AGNR edge and the GNR interior. The BOLS-TB derived Dirac-Fermi polarons agrees well with theoretical[190] and experimental observations for the edges and with what observed using STM/S from graphite vacancy.[40]
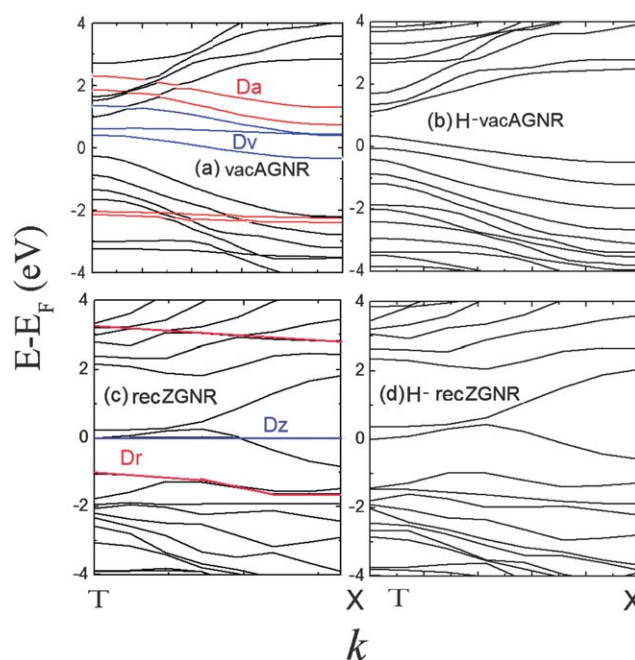
Fig. 17 Comparison of the DFT derived dispersions of AGNR edge and atomic vacancy (a) with and (b) without hydrogenation and the energy dispersions of ZGNR and rec-ZGNR (c) with and (d) without hydrogenation. The D_v (triple lines slightly above E_F in a) and D_z (one line at E_F) representing, respectively, the dangling σ-bond states of the vacancy and ZGNR edge; D_a (two pairs away from E F in a) and D_r (two lines away from E_F) representing the AGNR and the rec-ZGNR edges Pseudo-π-bond states. Hydrogenation removes all the D_a, D_v, and D_z completely with minus modification of the rest in the vicinity of E_F.

7.4 Edge discrimination and hydrogen annihilation

Fig. 18 compares the DFT calculated LDOS and the BOLS-TB derived spin difference (ΔS) counter plots under various edge conditions with and without hydrogenation. The DFT complements the BOLS-TB with derivatives summarized as follows:

i) The local magnetism is the summation of two contributions from the spin moments of the unpaired dangling sp^2 electrons and the nonbonding p_z electrons. The former is much stronger than the latter since the unpaired sp^2 is strongly localized and polarized whereas the p_z electron tends to itinerate as in graphite but partially entrapped by the edge quantum trap induced by BOLS correlation.

ii) Group I ((a) and (c)) demonstrates much stronger ΔS_V (0.7~1.0 electron/Å^3) than group II (0.05~0.1 electron/Å^3) because of the discussed electronic configurations and the effect of polarization and entrapment. The former arises not only from the localized dangling sp^2 electrons with the asymmetrically

polarized and alternative spin orientated nature but also from the partially trapped p_z electron; whereas for the latter, the sp^2 contribution is significantly attenuated by the quasi-π-bond formation since the sp^2 electron pairs offset the spin moments with each other.

iii) Hydrogenation reduces the ΔS_V of group I from 0.7~1.0 to 0.1~0.3 electron/Å^3 and unifies the orientations of the adjacent spins ((b) and (d)). The hydrogenation also turns the shape of the local spin from the asymmetric dumbbell-like sp^2 orbital to the spherical shaped p_z orbital in the xy plane, which confirms that the unpaired H 1s electron tends to pair and counteract with the dangling sp^2 electron more than the unpaired p_z electron. This finding may help in providing insight into the capability of graphite or graphene for hydrogen storage. The BOLS-TB derived 3D ΔS_E plot (down part in Fig. 5), distinguishing the contribution of p_z electrons and sp^2 electrons, also verify the above observations. Nonetheless, hydrogenation has no significant effects on group II.
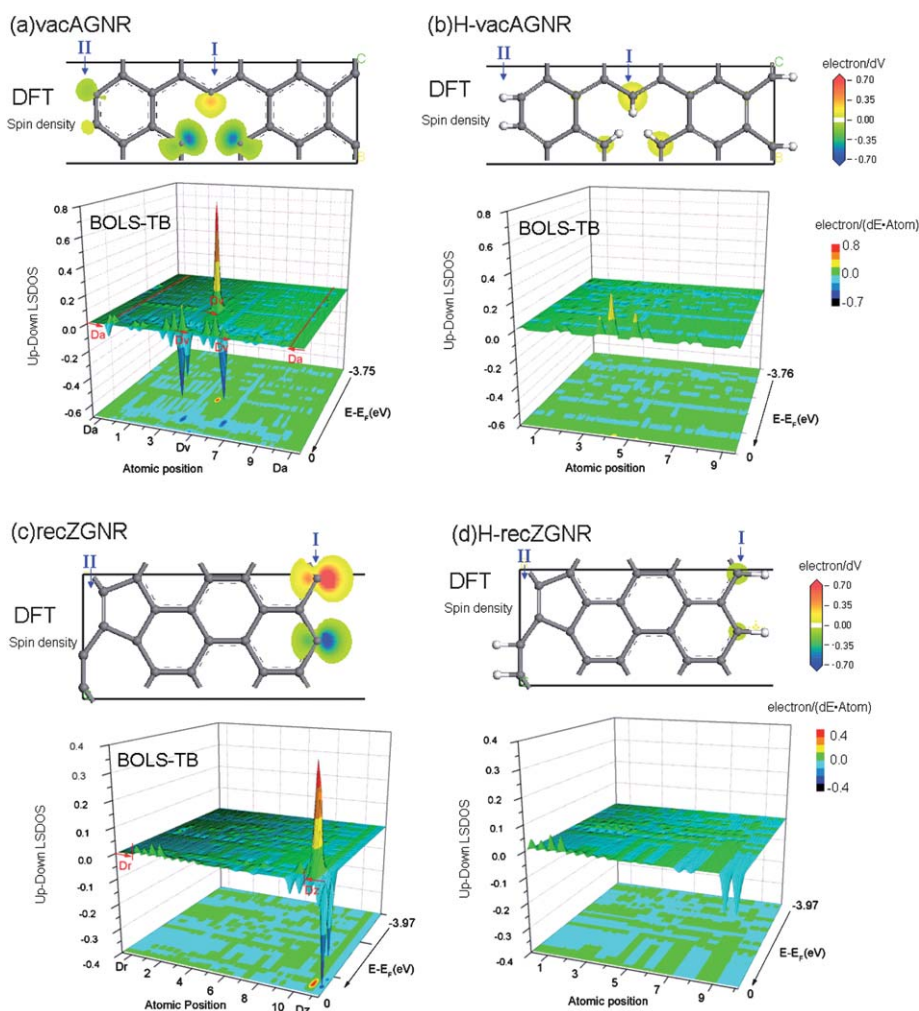
Fig. 18 Comparison of the DFT calculated LDOS and the BOLS-TB derived counterplots of spin difference for vacancy and AGNR edge (a) with and (b) without hydrogenation and for the rec-ZGNR (left side) and ZGNR (right) edge (c) with and (d) without hydrogenation. The results indicate that the vacancy and the ZGNR edge share the similarity with higher spin densities and that the AGNR and the rec-ZGNR edges share the similarity with lower spins because of the pseudo-π-bond formation. Hydrogenation turns the spin density from the asymmetric sp^2 dominance to the symmetric p_z dominance and alters the spin orientations from antiferromagnetic to parallel. The asymmetric dumbbell-shaped sp^2 LDOS evidences the polarization of the unpaired σ bonds and the spherical-shaped p_z LDOS represents the entrapment of the π electrons.

iv) The spin density of the vacAGNR edge is not ideally spherical, which results from the fact that the adjacent sp² electrons are not parallel and do not form a complete σ bond. The spin contribution of the sp² electrons has not been totally offset. Besides, only the closer side to the vacancy of vacAGNR presents spin density. It is attributed to the vacancy-enhanced edge quantum entrapment: the shorter and stronger bond induced by both vacancy and edge deepens the potential multi-well and hence the entrapment of charge and spin is enhanced.

v) In actual calculations performed within both first-principles and model tight binding approaches, broken bonds of edge carbon atoms are often saturated with hydrogen atoms as a rule and the dangling bonds do not contribute to the density of states in the vicinity of the Fermi energy, which annihilates the signatures of the edge states.

The magnetism of different edges and the atomic vacancy comply with the "hexagonal sublattice rule",[185] that is, the atomic vacancy and the ZGNR edge where the atoms surrounding the defect correspond to the same hexagonal sublattice distance manifest a large antiferromagnetic moment; while the AGNR and the rec-ZGNR edge atoms surrounding the defect correspond to different hexagonal sublattice present a weak magnetism because of the pseudo-π-bond coupling between the nearest dangling σ-bond electrons. The edge hydrogenation plays different roles in these two kinds of defects. Combined with the band structure dispersions in Fig. 17, the single-sharp D_z polarons are with energy at E_F and the triple D_v states are located above but the D_a and D_r behave more like the π and π* bands apart from the E_F at both sides. The former is the polarized dangling σ bond in nature and the latter more likes the π and π* bond.

7.5 Summary

A combination of the DFT and the BOLS-TB calculations confirmed that the high spins of Dirac-Fermi polarons are associated with atoms at sites surrounding atomic vacancies and ZGNR edges and the low spins with the AGNR and rec-ZGNR edges. Despite the spin value difference, the edge magnetism is dominated by the polarization of the unpaired sp² dangling bond electrons. The weak magnetism of the AGNR and rec-ZGNR edge atoms indicates the pseudo-π-bond formation between the nearest dangling σ-bond electrons to a certain extent along their edges. This finding also explain why the AGNR and rec-ZGNR edges perform more like semiconductor while the ZGNR and vacancy edges more like metal. The polarized dangling bond in ZGNR and vacancy originates the metallic, magnetic, and mobile Dirac-Fermi polarons and the pseudo-π-bond is responsible for the semiconductive nature of the AGNR and rec-ZGNR. It should be clear now why the edge discriminates the GNRs performance in the electronic, optic, magnetic and chemical and why the DFPs are massless and highly-mobile; what are the advantages and limitations in applications for the catalytic, H storage, sensor, *etc.* Further investigation is in progress.

VIII   GNR Raman shifts

● *The Raman D and 2D modes of GNR undergo red-shift from the reference point of the dimer vibration frequencies determined as 1273.0 and 2576.0 cm⁻¹ when the GNR layer is reduced or a tensile strain is applied.*

● *All the D, G, and 2D mode undergo red shift non-linearly under a tensile strain.*

● *The layer-number-reduction induced blue shift and the strain-induced splitting of the G mode may involve dipole-dipole interaction and the anisotropic stain due to the uniaxial strain.*

● *Scattering from the polarons at the ZGNR edge is suggested to lower the D band spectral intensity in comparison to that at the AGNR edge.*

● *Trends agreement between prediction and measurements of the z- and strain dependence of the D and 2D modes verify further the BOLS correlation mechanism.*

8.1   Layer number resolved and strain dependence of the Raman shift

Raman spectroscopy has been demonstrated to be a powerful tool in probing the lattice vibrational states and dynamics of GNRs and CNTs,[197–199] under the variation of the layer number,[200–203] strain,[204–206] doping, temperature,[207] edge chirality,[208–210] defect location,[211] substrate interaction,[212] hydrogenation,[213] structural orientation, light polarization angle with respect to the GNR surface plane.[214] There are three major Raman features of graphene: the G band (1580 cm⁻¹) arises from the in-plane vibrations of the sp² carbon atoms,[215] and the 2D band (2700 cm⁻¹) as a second-order process induced Raman feature.[216] In the presence of undercoordinated carbon atoms or the edge of graphene, another band located around 1350 cm⁻¹ can be observed, which is called the defect-induced band or D band. The intensity of the D band is one order higher at the armchair edge than that at the zigzag edge.[208,209]

Fig. 19 shows the frequency evolution of the Raman D and 2D bands with the layer-number of GNRs.[203,210] At a given excitation energy, the D and 2D peaks undergo a red-shift when the number of layers is reduced. When the GNR evolves from the bulk-graphite to monolayer GNR, the 2D peak evolves from 2714 to 2678 cm⁻¹ and the D peak changes from 1368 to 1344 cm⁻¹. However, the G band undergoes a blue-shift when the number of layers is reduced,[202] as illustrated in Fig. 20 with the numerical fitting[201] with the relations of: $\omega_G = 1581.6 + 5.5/n$, and $\omega_G = 1581.6 + 11/(1 + n^{1.6})$, as indicated.

Fig. 21 shows the Raman spectra of graphene under uniaxial tensile strain.[205] An obvious red-shift in G band and 2D band is observed on tensile strained graphene due to the elongation of carbon bonds, and such band shift was suggested to be linearly related to the strain. Another effect of the uniaxial strain on GNR is the G band splitting. The single G band in unstrained GNR is a result of doubly degenerate optical phonon mode. After the application of strain, lowering of the graphene symmetry splits the two phonon mode apart, causing the appearance of the two branches of the G bands in the strained graphene.[205,217,218]

Compared with the huge volume of Raman database collected under various conditions, the physical insight is in its infancy, in particular, from the perspective of bond formation, dissociation, relaxation and vibration under the given conditions. The objective of this section is to extend the BOLS consideration and the LBA approach to the typically observed Raman shift of GNR
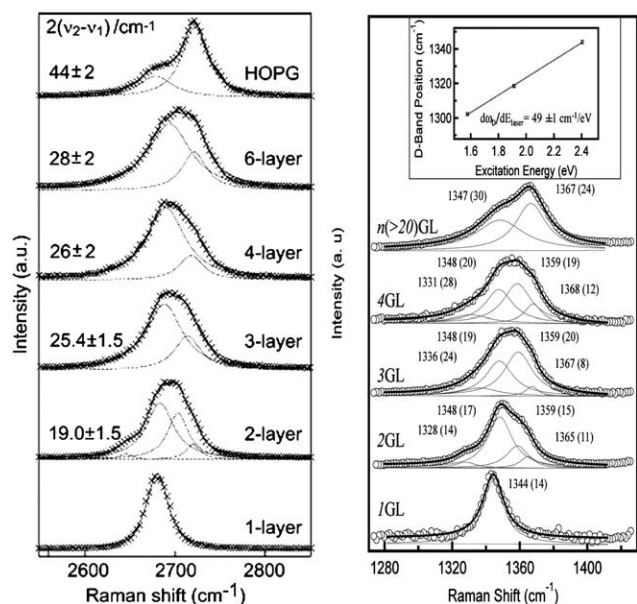
646 | *Energy Environ. Sci.*, 2011, **4**, 627–655

This journal is © The Royal Society of Chemistry 2011

Fig. 19 (left) The 2D Raman spectra of GNRs as a function of the number of layers varying from 1 to 6 along with HOPG as a bulk reference.[203] The single-peak position for the monolayer GNR is at 2678 ± 1 cm^{-1}; (right) Raman D-bands (edge excitation) for various n-layer films. (Inset) D-band dispersion for graphene; slope is 49 ± 1 cm^{-1} eV^{-1}.[210]
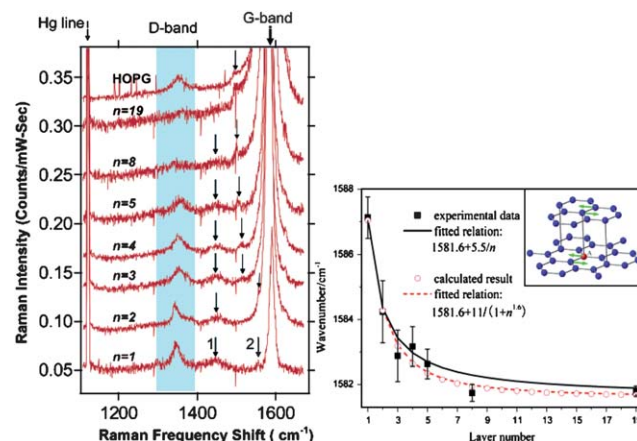

Fig. 20 (left) GNR layer-number dependence of the G peak shift;[202] and, (right) the numerical fit to the measurement with the relation of: $\omega_G = 1581.6 + 5.5/n$, and $\omega_G = 1581.6 + 11/(1 + n^{1.6})$, as indicated.[201]

under the variation of the number of layers and the strain. Modeling consideration of other factors is in progress.

8.2 BOLS formulation

When we consider a τ-dimensional solid containing numerous Bravais unit cells and each cell contains n atoms, there will be τn modes of vibrations. Among the τn modes there will be τ acoustic modes, LA, TA1, …, and TA(τ-1) and $\tau(n - 1)$ optical modes LO and TO. The acoustic modes represent the in-phase motion of the mass center of the unit cell or the entire solid as a whole. The long-range Coulomb interaction is responsible for the inter-cluster interaction.[219] From the BOLS perspective, the frequency of the Raman optical and acoustic modes follow the relations:[219,220]

$$\begin{cases} \omega_o(z) - \omega_o(1) \propto \dfrac{z}{d_z}\left(\dfrac{E_z}{\mu}\right)^{\frac{1}{2}} & \text{(optical mode)} \\[4mm] \omega_a(z) - \omega_a(1) \propto \dfrac{1}{K} & \text{(accoustic mode)} \end{cases} \quad (17)$$

where $\omega_o(z)$ is the vibration frequency of an atom with z neighbors. The $\omega_o(1)$ being the frequency of a dimer is the reference point from which the shift proceeds. The z, d_z, E_z, and μ represent the effective coordination number, bond length, bond energy, and the reduced mass of the dimer atoms: $\mu = m_1 m_2 / (m_1 + m_2)$. For the GNR without adsorption or isotope, the μ is a constant.

For the thickness-induced G peak blue shift in Fig. 20 follows roughly the BOLS derivatives given in eqn (17). Here we focus on the coordination, z, strain, ε, pressure, P, and temperature, T, dependence of the D and 2D optical modes.

Incorporating the considered variable of z, P, T, and ε into the optical mode in eqn (17), we have the relation,

$$\frac{\omega(z, P, T, \varepsilon) - \omega(1, P_0, T_0, 0)}{\omega(z_b, P_0, T_0, 0) - \omega(1, P_0, T_0, 0)} = \frac{z d_0}{d(z, P, T, \varepsilon)}\left(\frac{E(z, P, T, \varepsilon)}{E_0}\right)^{1/2}$$

where,

$$\begin{cases} d(z_b, P_0, T_0, 0) = d_0 \\ E(z_b, P_0, T_0, 0) = E_0 \end{cases}$$

and

$$\begin{cases} d(z, P, T, \varepsilon) = d_0\left[C_z\left(1 + \displaystyle\int_0^\varepsilon d\varepsilon\right)\left(1 + \displaystyle\int_{T_0}^T \alpha\, dt\right)\left(1 + \displaystyle\int_{P_0}^P \beta\, dp\right)\right] \\[4mm] E(z, P, T, \varepsilon) = E_0\left[C_z^{-m} - \dfrac{d_z^2 \displaystyle\int_0^\varepsilon \kappa(\varepsilon)\varepsilon\, d\varepsilon - \displaystyle\int_{T_0}^T \eta(t)dt - \displaystyle\int_{V_0}^V p(t)dv}{E_0}\right] \end{cases}$$
$$(18)$$

The thermal expansion coefficient, α, compressibility, β, specific heat, η, and the force constant, κ, are constant at higher temperatures or low pressures or distortion in the elastic regime.[219,221–223]

Taking z_b = 5.335 for graphite as reference, theoretical reproduction of the z- or layer-number dependence of the D and 2D modes frequency shift will lead to the quantification of $\omega(1)$:

$$\frac{\omega(z) - \omega(1)}{\omega(z_b) - \omega(1)} = \frac{z}{z_b}\left(\frac{C_z}{C_{zb}}\right)^{-(m/2+1)} = \frac{z}{z_b}\left(\frac{C_z}{C_{zb}}\right)^{-2.28} = C'(z, z_b) \quad (19)$$

From this relation, we can determine the $\omega(1)$, the bulk shift, $\omega(z_b) - \omega(1)$ and the z-dependent D and 2D Raman shift:

$$\omega(1) = \frac{\omega(z) - \omega(z_b)C'(z, z_b)}{1 - C'(z, z_b)}$$
$$\omega(z) = \omega(1) + [\omega(z_b) - \omega(1)]C'(z, z_b)$$
$$(20)$$

For the same GNR specimen with a constant effective z, the strain-effect is expressed as,

This journal is © The Royal Society of Chemistry 2011

Energy Environ. Sci., 2011, **4**, 627–655 | 647

$$\frac{\omega(z,\varepsilon)-\omega(1,0)}{\omega(z,0)-\omega(1,0)}=\frac{d_z}{d(z,\varepsilon)}\left(\frac{E(z,\varepsilon)}{E_z}\right)^{1/2}$$

$$=\left(1-\frac{d_z^2\int_0^\varepsilon\kappa(\varepsilon)\varepsilon\,d\varepsilon}{E_z}\right)^{1/2}\bigg/\left(1+\int_0^\varepsilon d\varepsilon\right)$$

$$=\left(1-\frac{d_z^2\int_0^\varepsilon\kappa(\varepsilon)\varepsilon\,d\varepsilon}{E_z}\right)^{1/2}\bigg/(1+\varepsilon)\cong\frac{(1-\kappa'\varepsilon^2)^{1/2}}{1+\varepsilon}$$

$$\kappa'=\kappa d_z^2/(2E_z)=\text{const.}$$

(21)

Likewise, for the thermal and pressure effects, we have,[224,225]

$$\frac{\omega(z,T)-\omega(1,T_0)}{\omega(z,T_0)-\omega(1,T_0)}=\left(1-\frac{\int_{T_0}^T\eta(t)\,dt}{C_z^{-m}E_b}\right)^{1/2}\bigg/\left(1+\int_{T_0}^T\alpha\,dt\right)$$

$$\frac{\omega(z,P)-\omega(1,P_0)}{\omega(z,P_0)-\omega(1,P_0)}=\left(1-\frac{\int_{V_0}^V p(t)\,dv}{C_z^{-m}E_b}\right)^{1/2}\bigg/\left(1+\int_{P_0}^P\beta\,dp\right)$$

(22)

Theoretical unification of Raman shift on these variables allow us to extract quantitative information about the $\omega(1)$, α, β, κ, $\theta_D(\eta)$, and the binding energy E_b, which should be the pursuit of our practice.

8.3 Derivatives

In sections 3 and 4, we have determined that for the monolayer GNR, $z=3(2.97)$, and $z_b=5.335$ for graphite bulk. For 2, 3, and 10 layers, $z\approx=3.20$, 3.45 and 4.05, respectively. With the given Raman frequencies of the 2D peak shifting from 2714 to 2678 cm^{-1} and the D peak from 1368 to 1344 cm^{-1} when the graphite turns to monolayer GNR, we have

$$C'(3.0,5.335)=\frac{z'}{z}\left(\frac{C_z}{C_{z'}}\right)^{-2.28}=\frac{3.0}{5.335}\left(\frac{0.8147}{0.9220}\right)^{-2.28}=0.7458$$

Therefore, from eqn (20), we can obtain,

$$\omega(1)=\frac{\omega(3.0)-\omega(5.335)C'(3.0,5.335)}{1-C'(3.0,5.335)}$$

$$=\begin{cases}\dfrac{1344-1368\times0.7458}{1-0.7458}=1273.6(cm^{-1}) & \text{(D peak)}\\[2mm]\dfrac{2678-2714\times0.7458}{1-0.7458}=2572.4(cm^{-1}) & \text{(2D peak)}\end{cases}$$

(23)

And the z-dependent Raman D and 2D red shift,

$$\omega(z)=\omega(1)+[\omega(z_b)-\omega(1)]C'(z,z_b)$$

$$=\begin{cases}1273.6+(1368.0-1273.6)C'(z,5.335) & \text{(D)}\\2572.1+(2714.0-2572.4)C'(z,5.335) & \text{(2D)}\end{cases}$$

(24)

Combining eqn (19) and eqn (21), we have the coordination- and strain-dependent Raman shift of GNR:

$$\omega(z,\varepsilon)=\omega(1,0)+[\omega(z,0)-\omega(1,0)]\frac{(1-\kappa'\varepsilon^2)^{1/2}}{(1+\varepsilon)}$$

$$=\omega(1,0)+[\omega(5.335,0)-\omega(1,0)]C'(z,5.335)\frac{(1-\kappa'\varepsilon^2)^{1/2}}{(1+\varepsilon)}$$

$$=C'(z,5.335)\frac{(1-\kappa'\varepsilon^2)^{1/2}}{1+\varepsilon}\begin{cases}\times94.4+1273.6 & \text{(D)}\\\times141.9+2572.4 & \text{(2D)}\end{cases}(cm^{-1})$$
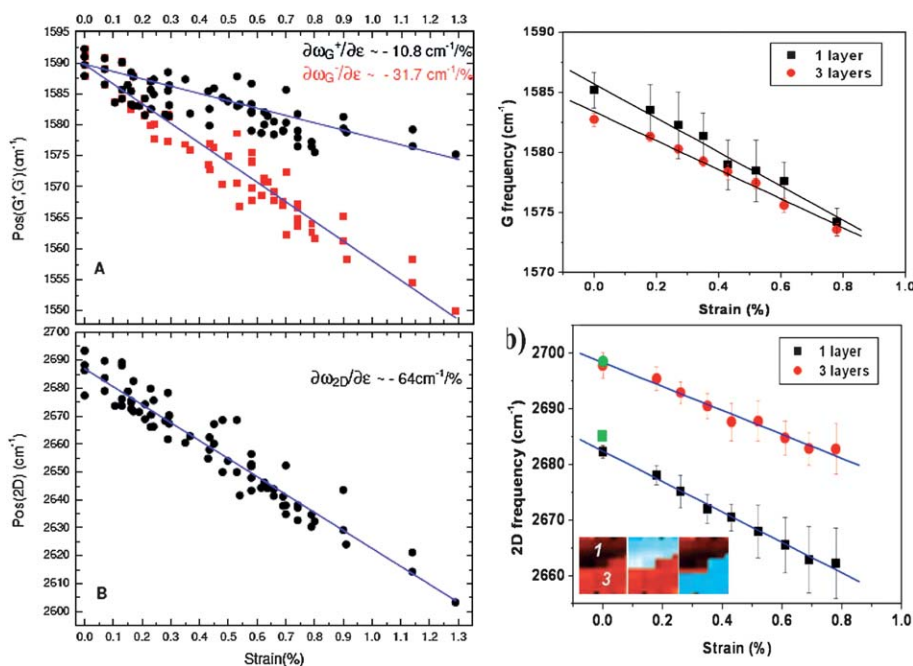
(25)

Fig. 21 Uniaxial strain induced red-shift of Raman frequencies of the (a, c) G$^+$ and G$^-$ and (b, d) 2D.[205,218]
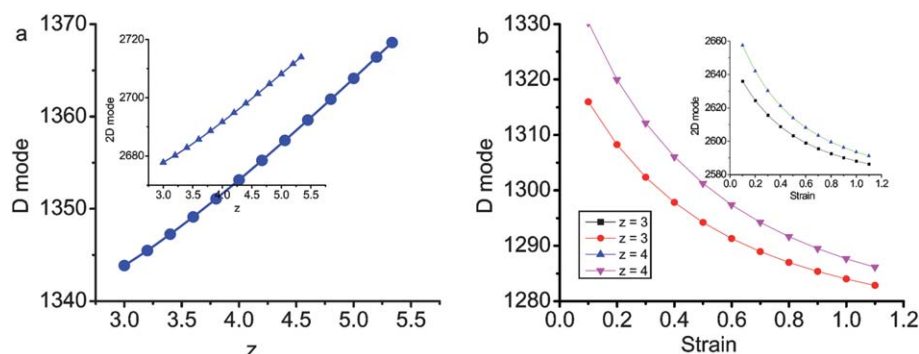
Fig. 22 BOLS derived (a) z- and (b) strain-dependent Raman shift of the D and 2D modes with derivatives of the dimer vibration frequency, $\omega(1)$ and the $\kappa' = \kappa d_z^2/(2E_z) = 0.30$.

$(\kappa' = \kappa d_z^2/(2E_z)$ is the adjustable parameter in the theoretical reproduction of the measurement).

Fig. 22 compares the BOLS derived z- and strain-dependence of the Raman shift of the D and 2D modes derived from eqns (24) and (25). The calculated trends are in line with the measurements as given in Fig. 19 and Fig. 21.

It is easy to understand that the intensity sensitivity of the D band to the edge type as the scattering of the incident light by the Dirac-Fermi polarons at the zigzag edge is much stronger and hence the intensity at the ZGNR edge is substantially lower than that from the AGNR edge. Regarding the layer-number-reduction induced blue shift and the strain-induced splitting of the G band is beyond the scope of the BOLS correlation mechanism at the present moment. However, dipole interaction and the Poisson ratio caused non-uniform strain may contribute. Further investigation on these issues is in progress.

8.4 Summary

In summary, consistency between the prediction and the observations on the layer (z) and strain dependence of the Raman D and 2D mode frequency shift evidence further the validity of the BOLS correlation mechanism. The spectral intensity sensitivity of the D band to the edge chirality is found to be due to the presence of the Dirac-Fermi polarons that scattering strongly the incident light and hence lower the Raman intensity. Furthermore, the reference points from where the Raman frequency shifts have been determined as 1273.0 and 2571.6 for the D and 2D modes. Further investigation on the temperature, pressure, and the G band splitting and G band blue shift would be more challenging.

IX Conclusion

9.1 Achievement

A combination of the BOLS theory, experimental observations, and the DFT and BOLS-TB calculations has enabled us to gain consistent insight into the fascinations demonstrated by CNTs and GNRs from the perspective of bond and nonbond formation, dissociation, relaxation and vibration, and the associated energetics and dynamics of charge repopulation, polarization, densification, and localization. Major progresses are summarized as follows:

i) Theoretical reproduction of the elastic modulus enhancement and melting point depression of SWCNT revealed that the C–C bond of SWCNT and monolayer graphene is 0.142 nm thick and 0.125 nm long. Bonds between 3-coordinated atoms are shortened by 18.5% and strengthened by 68%, and bonds between 2-coordinated edge atoms are shortened by 30% and strengthened by 152% with respect to those of diamond. The elastic modulus is 2.5 times that of the bulk. The elastic modulus is proportional to the local binding energy density and the chemical and thermal stability depends on the atomic cohesive energy.

ii) With the quantities derived from the matching of elastic modulus enhancement and melting point depression, we have been able to reproduce the measured C 1s energy shift of GNR, graphite, and diamond by combining the BOLS correlation and the tight-binding considerations. Reproduction has led to the quantification of the C 1s energy of an isolated atom as 282.57 eV and the CN-resolved shift of: $E_{1s}(z) = 282.57 + 1.32C_z^{-2.56}(eV)$. The undercoordination induced simultaneous positive C 1s shift and the work function reduction of graphene and C_{60} evidence the BOLS expectation of the broken-bond-induced local quantum entrapment and densification of energy and electrons and the consequent nonbonding electron polarization.

iii) An atomic-scale, zone-selective photoelectron spectroscopic purification has enabled clarification of the mechanism of graphitic Dirac-Fermi polarons generation and retention as arising from the polarization of the unpaired dangling-bond electrons by the densely, deeply, and locally entrapped bonding and core electrons. This technique also allows us to clarify the defect and surface states in the entire energy range and the correlations.

iv) The ZGNR edge and atomic vacancy selective generation of the Dirac-Fermi polarons results from the dangling σ-bond electron isolation and polarization along the hexagonal sublattice with identical distance while the alternative distance of atoms along the AGNR and rec-ZGNR edges may favor the pseudo-π-bond formation, which also explains why the former are metallic and the latter semiconductive. The band gap opening takes place as the pseudo-π-bond minimizes the mid-gap impurity states.

v) The band gap generation is dominated by the edge quantum entrapment, instead of confinement, due to the under-coordination-induced local bond strain and strengthening. The inconsistency between DFT calculated and the measured E_G expansion arises from the impurity midgap states meditation. Calculations deals with the ideal situation while measurement measure the true situation of exciton generation from the upper edge of the midgap impurity states to the valence band.

vi) High densities of spins are associated with Dirac-Fermi polarons because of the polarized dangling σ bond electrons,

which present only to the ZGNR edges and vacancies. H–C bond formation at edge annihilates the magnetism and turns the antiferromagnetism to paramagnetic.

vii) The layer-number, strain, pressure, and temperature induced Raman shift can be reconciled using the BOLS relation and the response of bond length and bond energy to the applied stimuli.

9.2 Perspectives

The understanding herewith may extend to other situations with large proportion of under-coordinated atoms such as the densification and localization of electrons with lowered binding energy in the potential traps as observed as defect states, chain end states,[226–228] terrace edge states, and surface states. The globally quantum entrapments exist at such undercoordinated atomic sites but the polarization is subject to the presence of nonbonding electrons.[89] If both polarization and entrapment effect coexist, the sites with coordination imperfection are surrounded with the densely, locally, and deeply entrapped charge and energy and the polarization caps. The impact of such local energetic and electronic configuration would be profoundly enormous.

For instances, the similarity of the purified core band of graphite surface to those obtained from the acceptor-type catalyst of Pt adatoms CuPd alloys and the core band of graphite surface with defects to the donor-like catalysts of Rh adatoms and AgPd alloys[151,156] suggest that graphite surface with and without vacancy defect may serve, respectively, as an acceptor- and a donor-type catalyst because of the respective polarization and entrapment. It is suggested that the GNRs with zigzag edges serve the same to atomic vacancy and the AGNR and rec-ZGNR to the flat surface in the catalytic reactions and further verification is necessary. The tendency of the C–H bond formation with the GNR edge dangling σ-bond and the entrapped π-bond electrons may provide insight into the capacity and limitation of hydrogen storage in the GNRs and CNTs.[8] It appears that under the normal circumstance (pressure and temperature) H tends to bond to the atomic vacancy and the ZGNR edges than to the AGNR or the rec-ZGNR edges. Edge chemisorption of various adsorbates forms an important and effective way to tune the physical properties of GNRs.[229] In the density-functional theory calculations, Hu *et al*[230] found that the structure of the edge-oxygenated GNR is more stable than those with naked edge, and the stability is enhanced when the GNR become narrower; applying an in-plane electric field across the AGNR can modulate the band gap through the process of entrapment and polarization. The polarized nonbonding states or the Dirac-Fermi polarons are expected to serve as the main vehicles for the topological insulators, high-T_C super conductors, and thermo-electronic materials, because of the massless and highly mobile nature of the carriers. These DFPs lowers the local work function that benefits the cold cathode electron emission,[146] and therefore, the ZGNR without hydrogenation could be good candidate for field emitters.[231–233] The impact of atomic undercoordination and the associated quantum entrapment and polarization for the CNTs and GNRs are indeed profound, which originates the unusual performance of the undercoordinated carbon allotropes. Further investigation focusing on the undercoordination-induced quantum entrapment and densification of charge and energy and their consequence on the polarization of nonbonding

states and find them practical applications would be even more exciting and rewarding.

Note added at proof

As our paper was in proof preparation, we learned of the discovery[234] that the mechanical strength of graphene is higher for high angle grain boundaries (GB) even though they have a higher density of defects (5- and 7-membered rings forming the GB) than for low angle grain boundaries, because of the particular ring bonds and their elongation dynamics. This finding is counter to standard expectations based on continuum mechanics as explained in ref. 234. This finding and the associated mechanism may provide possible solution to the long-standing puzzle[235] of the defect-density modulated mechanical strength of a bulk as well. The defects provide not only centers initiating the mechanical failure but also sites for energy pinning as the mechanical strength is proportional to the binding energy density.[94]

Acknowledgements

References

1 S. Iijima, Helical microtubes of graphitic carbon, *Nature*, 1991, **354**, 56–8.

2 H. J. Dai, J. H. Hafner, A. G. Rinzler, D. T. Colbert and R. E. Smalley, Nanotubes as nanoprobes in scanning probe microscopy, *Nature*, 1996, **384**, 147–50.

3 P. G. Collins and A. Zettl, Unique characteristics of cold cathode carbon-nanotube-matrix field emitters, *Phys. Rev. B: Condens. Matter Mater. Phys. Mater.: Condens. Matter*, 1997, **55**, 9391–9.

4 W. A. Deheer, A. Chatelain and D. Ugarte, Acarbon nanotube field-emission electron cource, *Science*, 1995, **270**, 1179–80.

5 A. Bachtold, P. Hadley, T. Nakanishi and C. Dekker, Logic circuits with carbon nanotube transistors, *Science*, 2001, **294**, 1317–20.

6 J. Lee, H. Kim, S. J. Kahng, G. Kim, Y. W. Son, J. Ihm, H. Kato, Z. W. Wang, T. Okazaki, H. Shinohara and Y. Kuk, Bandgap modulation of carbon nanotubes by encapsulated metallofullerenes, *Nature*, 2002, **415**, 1005–8.

7 A. C. Dillon, K. M. Jones, T. A. Bekkedahl, C. H. Kiang, D. S. Bethune and M. J. Heben, Storage of hydrogen in single-walled carbon nanotubes, *Nature*, 1997, **386**, 377–9.

8 C. Z. Wu and H. M. Cheng, Effects of carbon on hydrogen storage performances of hydrides, *J. Mater. Chem.*, 2010, **20**, 5390–400.

9 Y. Y. Xia, J. Z. H. Zhu, M. W. Zhao, F. Li, B. D. Huang, Y. J. Ji, X. D. Liu, Z. Y. Tan, C. Song and Y. Y. Yin, Enhancement of hydrogen physisorption on single-walled carbon nanotubes resulting from defects created by carbon bombardment, *Phys. Rev. B: Condens. Matter Mater. Phys. Mater. Phys.: Condens. Matter*, 2005, **71**, 075412.

10 C. Liu, Y. Chen, C. Z. Wu, S. T. Xu and H. M. Cheng, Hydrogen storage in carbon nanotubes revisited, *Carbon*, 2010, **48**, 452–5.

11 P. G. Collins, K. Bradley, M. Ishigami and A. Zettl, Extreme oxygen sensitivity of electronic properties of carbon nanotubes, *Science*, 2000, **287**, 1801–4.

12 J. Kong, N. R. Franklin, C. W. Zhou, M. G. Chapline, S. Peng, K. J. Cho and H. J. Dai, Nanotube molecular wires as chemical sensors, *Science*, 2000, **287**, 622–5.

13 G. Centi and S. Perathoner, Problems and perspectives in nanostructured carbon-based electrodes for clean and sustainable energy, *Catal. Today*, 2010, **150**, 151–62.

14 G. L. Che, B. B. Lakshmi, E. R. Fisher and C. R. Martin, Carbon nanotubule membranes for electrochemical energy storage and production, *Nature*, 1998, **393**, 346–9.

15 C. Liu, F. Li, L. P. Ma and H. M. Cheng, Advanced Materials for Energy Storage, *Adv. Mater.*, 2010, **22**, E28.

16 E. H. T. Teo, W. K. P. Yung, D. H. C. Chua and B. K. Tay, A carbon nanomattress: A new nanosystem with intrinsic, tunable, damping properties, *Adv. Mater.*, 2007, **19**, 2941.

17 K. S. Novoselov, A. K. Geim, S. V. Morozov, D. Jiang, Y. Zhang, S. V. Dubonos, I. V. Grigorieva and A. A. Firsov, Electric field effect in atomically thin carbon films, *Science*, 2004, **306**, 666–9.

18 K. Nakada, M. Igami, K. Wakabayashi and M. Fujita, Localized pi Electronic Edge State in Nanographite, *Molecular Crystals and Liquid Crystals Science and Technology Section a-Molecular Crystals and Liquid Crystals*, 1998, **310**, 225–30.

19 C. Q. Sun, S. Y. Fu and Y. G. Nie, Dominance of Broken Bonds and Unpaired Nonbonding pi-Electrons in the Band Gap Expansion and Edge States Generation in Graphene Nanoribbons, *J Chem Phys C*, 2008, **112**, 18927–34.

20 O. Hod, V. Barone, J. E. Peralta and G. E. Scuseria, Enhanced half-metallicity in edge-oxidized zigzag graphene nanoribbons, *Nano Lett.*, 2007, **7**, 2295–9.

21 N. Levy, S. A. Burke, K. L. Meaker, M. Panlasigui, A. Zettl, F. Guinea, A. H. C. Neto and M. F. Crommie, Strain-Induced Pseudo-Magnetic Fields Greater Than 300 Tesla in Graphene Nanobubbles, *Science*, 2010, **329**, 544–7.

22 R. Prasher, Graphene Spreads the Heat, *Science*, 2010, **328**, 185–6.

23 Y. M. Lin, C. Dimitrakopoulos, K. A. Jenkins, D. B. Farmer, H. Y. Chiu, A. Grill and P. Avouris, 100-GHz Transistors from Wafer-Scale Epitaxial Graphene, *Science*, 2010, **327**, 662.

24 D. Hsieh, Y. Xia, D. Qian, L. Wray, J. H. Dil, F. Meier, J. Osterwalder, L. Patthey, J. G. Checkelsky, N. P. Ong, A. V. Fedorov, H. Lin, A. Bansil, D. Grauer, Y. S. Hor, R. J. Cava and M. Z. Hasan, A tunable topological insulator in the spin helical Dirac transport regime, *Nature*, 2009, **460**, 1101–U59.

25 A. K. Geim, Graphene: Status and Prospects, *Science*, 2009, **324**, 1530–4.

26 T. W. Odom, J. L. Huang, P. Kim and C. M. Lieber, Atomic structure and electronic properties of single-walled carbon nanotubes, *Nature*, 1998, **391**, 62–4.

27 A. H. Castro Neto, F. Guinea, N. M. R. Peres, K. S. Novoselov and A. K. Geim, The electronic properties of graphene, *Rev. Mod. Phys.*, 2009, **81**, 109–62.

28 M. Konig, S. Wiedmann, C. Brune, A. Roth, H. Buhmann, L. W. Molenkamp, X. L. Qi and S. C. Zhang, Quantum spin hall insulator state in HgTe quantum wells, *Science*, 2007, **318**, 766–70.

29 D. Hsieh, D. Qian, L. Wray, Y. Xia, Y. S. Hor, R. J. Cava and M. Z. Hasan, A topological Dirac insulator in a quantum spin Hall phase, *Nature*, 2008, **452**, 970–U5.

30 R. Yu, W. Zhang, H. J. Zhang, S. C. Zhang, X. Dai and Z. Fang, Quantized Anomalous Hall Effect in Magnetic Topological Insulators, *Science*, 2010, **329**, 61–4.

31 T. Zhang, P. Cheng, X. Chen, J. F. Jia, X. C. Ma, K. He, L. L. Wang, H. J. Zhang, X. Dai, Z. Fang, X. C. Xie and Q. K. Xue, Experimental Demonstration of Topological Surface States Protected by Time-Reversal Symmetry, *Phys. Rev. Lett.*, 2009, **103**, 266803.

32 K. S. Novoselov, A. K. Geim, S. V. Morozov, D. Jiang, M. I. Katsnelson, I. V. Grigorieva, S. V. Dubonos and A. A. Firsov, Two-dimensional gas of massless Dirac fermions in graphene, *Nature*, 2005, **438**, 197–200.

33 N. Tombros, C. Jozsa, M. Popinciuc, H. T. Jonkman and B. J. van Wees, Electronic spin transport and spin precession in single graphene layers at room temperature, *Nature*, 2007, **448**, 571–U4.

34 K. S. Novoselov, Z. Jiang, Y. Zhang, S. V. Morozov, H. L. Stormer, U. Zeitler, J. C. Maan, G. S. Boebinger, P. Kim and A. K. Geim, Room-temperature quantum hall effect in graphene, *Science*, 2007, **315**, 1379.

35 L. Brey and H. A. Fertig, Electronic states of graphene nanoribbons studied with the Dirac equation, *Phys. Rev. B: Condens. Matter Mater. Phys. Mater. Phys.*, 2006, **73**, 235411.

36 F. M. D. Pellegrino, G. G. N. Angilella and R. Pucci, Strain effect on the optical conductivity of graphene, *Phys. Rev. B: Condens. Matter Mater. Phys. Mater. Phys.*, 2010, **81**, 035411.

37 H. B. Heersche, P. Jarillo-Herrero, J. B. Oostinga, L. M. K. Vandersypen and A. F. Morpurgo, Bipolar supercurrent in graphene, *Nature*, 2007, **446**, 56–9.

38 C. Girit, V. Bouchiat, O. Naamanth, Y. Zhang, M. F. Crommie, A. Zetti and I. Siddiqi, Tunable Graphene do Superconducting Quantum Interference Device, *Nano Lett.*, 2009, **9**, 198–9.

39 A. M. Black-Schaffer and S. Doniach, Possibility of measuring intrinsic electronic correlations in graphene using a d-wave contact Josephson junction, *Phys. Rev. B: Condens. Matter Mater. Phys. Mater. Phys.: Condens. Matter*, 2010, **81**, 014517.

40 M. M. Ugeda, I. Brihuega, F. Guinea and J. M. Gómez-Rodríguez, Missing Atom as a Source of Carbon Magnetism, *Phys. Rev. Lett.*, 2010, **104**, 096804.

41 T. Matsui, H. Kambara, Y. Niimi, K. Tagami, M. Tsukada and H. Fukuyama, STS Observations of Landau Levels at Graphite Surfaces, *Phys. Rev. Lett.*, 2005, **94**, 226403.

42 G. Li and E. Y. Andrei, Observation of Landau levels of Dirac fermions in graphite, *Nat. Phys.*, 2007, **3**, 623–7.

43 Y. Niimi, T. Matsui, H. Kambara, K. Tagami, M. Tsukada and H. Fukuyama, Scanning tunneling microscopy and spectroscopy of the electronic local density of states of graphite surfaces near monoatomic step edges, *Phys. Rev. B: Condens. Matter Mater. Phys. Mater. Phys.: Condens. Matter*, 2006, **73**, 085421–8.

44 Y. Niimi, H. Kambara and H. Fukuyama, Localized Distributions of Quasi-Two-Dimensional Electronic States near Defects Artificially Created at Graphite Surfaces in Magnetic Fields, *Phys. Rev. Lett.*, 2009, **102**, 026803–4.

45 T. Enoki, Y. Kobayashi and K. I. Fukui, Electronic structures of graphene edges and nanographene, *Int. Rev. Phys. Chem.*, 2007, **26**, 609–45.

46 C. O. Girit, J. C. Meyer, R. Erni, M. D. Rossell, C. Kisielowski, L. Yang, C. H. Park, M. F. Crommie, M. L. Cohen, S. G. Louie and A. Zettl, Graphene at the Edge: Stability and Dynamics, *Science*, 2009, **323**, 1705–8.

47 D. L. Miller, K. D. Kubista, G. M. Rutter, M. Ruan, W. A. de Heer, P. N. First and J. A. Stroscio, Observing the Quantization of Zero Mass Carriers in Graphene, *Science*, 2009, **324**, 924–7.

48 Y. W. Son, M. L. Cohen and S. G. Louie, Energy gaps in graphene nanoribbons, *Phys. Rev. Lett.*, 2006, **97**, 216803.

49 M. Fujita, K. Wakabayashi, K. Nakada and K. Kusakabe, Peculiar Localized State at Zigzag Graphite Edge, *J. Phys. Soc. Jpn.*, 1996, **65**, 1920–3.

50 A. K. Geim and K. S. Novoselov, The rise of graphene, *Nat. Mater.*, 2007, **6**, 183–91.

51 M. A. H. Vozmediano, M. P. Lopez-Sancho, T. Stauber and F. Guinea, Local defects and ferromagnetism in graphene layers, *Phys. Rev. B: Condens. Matter Mater. Phys. Mater. Phys.: Condens. Matter*, 2005, **72**, 155121.

52 S. Y. Zhou, G. H. Gweon, J. Graf, A. V. Fedorov, C. D. Spataru, R. D. Diehl, Y. Kopelevich, D. H. Lee, S. G. Louie and A. Lanzara, First direct observation of Dirac fermions in graphite, *Nat. Phys.*, 2006, **2**, 595–9.

53 A. De Martino, L. Dell'Anna and R. Egger, Magnetic confinement of massless Dirac fermions in graphene, *Phys. Rev. Lett.*, 2007, **98**, 066802.

54 K. Nomura and A. H. MacDonald, Quantum transport of massless dirac fermions, *Phys. Rev. Lett.*, 2007, **98**, 076602.

55 J. Yan, Y. B. Zhang, P. Kim and A. Pinczuk, Electric field effect tuning of electron-phonon coupling in graphene, *Phys. Rev. Lett.*, 2007, **98**, 166802.

56 G. H. Li, A. Luican and E. Y. Andrei, Scanning Tunneling Spectroscopy of Graphene on Graphite, *Phys. Rev. Lett.*, 2009, **102**, 176804.

57 X. Z. Yan and C. S. Ting, Weak localization of Dirac fermions in graphene, *Phys. Rev. Lett.*, 2008, **101**, 126801.

58 L. Yang, C.-H. Park, Y.-W. Son, M. L. Cohen and S. G. Louie, Quasiparticle Energies and Band Gaps in Graphene Nanoribbons, *Phys. Rev. Lett.*, 2007, **99**, 186801.

59 K. Nakada, M. Fujita, G. Dresselhaus and M. S. Dresselhaus, Edge state in graphene ribbons: Nanometer size effect and edge shape

dependence, *Phys. Rev. B: Condens. Matter Mater. Phys. Mater. Phys.: Condens. Matter* , 1996, **54**, 17954–61.

60 D. Gunlycke and C. T. White, Tight-binding energy dispersions of armchair-edge graphene nanostrips, *Phys. Rev. B: Condens. Matter Mater. Phys. Mater. Phys.: Condens. Matter* , 2008, **77**, 115116.

61 M. Y. Han, B. Ozyilmaz, Y. B. Zhang and P. Kim, Energy band-gap engineering of graphene nanoribbons, *Phys. Rev. Lett.*, 2007, **98**, 206805.

62 S. S. Yu, Q. B. Wen, W. T. Zheng and Q. Jiang, Electronic properties of graphene nanoribbons with armchair-shaped edges, *Mol. Simul.*, 2008, **34**, 1085–90.

63 P. Koskinen, S. Malola and H. Hakkinen, Evidence for graphene edges beyond zigzag and armchair, *Phys. Rev. B: Condens. Matter Mater. Phys. Mater. Phys.: Condens. Matter* , 2009, **80**, 073401.

64 E. Hernandez, C. Goze, P. Bernier and A. Rubio, Elastic properties of C and BxCyNz composite nanotubes, *Phys. Rev. Lett.*, 1998, **80**, 4502–5.

65 M. F. Yu, O. Lourie, M. J. Dyer, K. Moloni, T. F. Kelly and R. S. Ruoff, Strength and breaking mechanism of multiwalled carbon nanotubes under tensile load, *Science*, 2000, **287**, 637–40.

66 M. F. Yu, B. S. Files, S. Arepalli and R. S. Ruoff, Tensile loading of ropes of single wall carbon nanotubes and their mechanical properties, *Phys. Rev. Lett.*, 2000, **84**, 5552–5.

67 M. M. J. Treacy, T. W. Ebbesen and J. M. Gibson, Exceptionally high Young's modulus observed for individual carbon nanotubes, *Nature*, 1996, **381**, 678–80.

68 J. P. Salvetat, A. J. Kulik, J. M. Bonard, G. A. D. Briggs, T. Stockli, K. Metenier, S. Bonnamy, F. Beguin, N. A. Burnham and L. Forro, Elastic modulus of ordered and disordered multiwalled carbon nanotubes, *Adv. Mater.*, 1999, **11**, 161–5.

69 J. P. Salvetat, G. A. D. Briggs, J. M. Bonard, R. R. Bacsa, A. J. Kulik, T. Stockli, N. A. Burnham and L. Forro, Elastic and shear moduli of single-walled carbon nanotube ropes, *Phys. Rev. Lett.*, 1999, **82**, 944–7.

70 E. T. Thostenson, Z. F. Ren and T. W. Chou, Advances in the science and technology of carbon nanotubes and their composites: a review, *Compos. Sci. Technol.*, 2001, **61**, 1899–912.

71 B. I. Yakobson, C. J. Brabec and J. Bernholc, Nanomechanics of carbon tubes: Instabilities beyond linear response, *Phys. Rev. Lett.*, 1996, **76**, 2511–4.

72 W. Liu, L. M. Jawerth, E. A. Sparks, M. R. Falvo, R. R. Hantgan, R. Superfine, S. T. Lord and M. Guthold, Fibrin fibers have extraordinary extensibility and elasticity, *Science*, 2006, **313**, 634.

73 Z. C. Tu and Z. C. Ou-Yang, Dimensional crossover of dilute neon inside infinitely long single-walled carbon nanotubes viewed from specific heats, *Phys. Rev. B: Condens. Matter Mater. Phys. Mater. Phys.: Condens. Matter* , 2003, **68**, 153403.

74 B. An, S. Fukuyama, K. Yokogawa and M. Yoshimura, Surface superstructure of carbon nanotubes on highly oriented pyrolytic graphite annealed at elevated temperatures, *Japan J Applied Physics*, 1997, 3809–11.

75 P. Nikolaev, A. Thess, A. G. Rinzler, D. T. Colbert and R. E. Smalley, Diameter doubling of single-wall nanotubes, *Chem. Phys. Lett.*, 1997, **266**, 422–6.

76 P. M. Ajayan, M. Terrones, A. de la Guardia, V. Huc, N. Grobert, B. Q. Wei, H. Lezec, G. Ramanath and T. W. Ebbesen, Nanotubes in a flash - Ignition and reconstruction, *Science*, 2002, **296**, 705.

77 S. Reich, J. Maultzsch, C. Thomsen and P. Ordejo, Tight-binding description of graphene, *Phys. Rev. B: Condens. Matter Mater. Phys. Mater. Phys.*, 2002, **66**, 035412.

78 I. Zanella, S. Guerini, S. B. Fagan, J. Mendes and A. G. Souza, Chemical doping-induced gap opening and spin polarization in graphene, *Phys. Rev. B: Condens. Matter Mater. Phys. Mater. Phys.: Condens. Matter* , 2008, **77**, 073404.

79 E. Rotenberg, A. Bostwick, T. Ohta, J. L. McChesney, T. Seyller and K. Horn, Origin of the energy bandgap in epitaxial graphene, *Nat. Mater.*, 2008, **7**, 258–9.

80 Z. F. Wang, Q. X. Li, H. X. Zheng, H. Ren, H. B. Su, Q. W. Shi and J. Chen, Tuning the electronic structure of graphene nanoribbons through chemical edge modification: A theoretical study, *Phys. Rev. B: Condens. Matter Mater. Phys. Mater. Phys.: Condens. Matter* , 2007, **75**, 113406.

81 S. Y. Zhou, D. A. Siegel, A. V. Fedorov, F. El Gabaly, A. K. Schmid, A. H. C. Neto, D. H. Lee and A. Lanzara, Origin of the energy bandgap in epitaxial graphene - Reply, *Nat. Mater.*, 2008, **7**, 259–60.

82 S. Y. Zhou, G. H. Gweon, A. V. Fedorov, P. N. First, W. A. De Heer, D. H. Lee, F. Guinea, A. H. C. Neto and A. Lanzara,

Substrate-induced bandgap opening in epitaxial graphene, *Nat. Mater.*, 2007, **6**, 770–5.

83 G. Gui, J. Li and J. X. Zhong, Band structure engineering of graphene by strain: First-principles calculations, *Phys. Rev. B: Condens. Matter Mater. Phys. Mater. Phys.: Condens. Matter*, 2008, **78**, 075435.

84 C. L. Kane and E. J. Mele, Quantum spin Hall effect in graphene, *Phys. Rev. Lett.*, 2005, **95**, 226801.

85 T. Kondo, Y. Honma, J. Oh, T. Machida and J. Nakamura, Edge states propagating from a defect of graphite: Scanning tunneling spectroscopy measurements, *Phys. Rev. B: Condens. Matter Mater. Phys. Mater. Phys.: Condens. Matter* , 2010, **82**, 153414.

86 K. J. Kim, H. Lee, J. H. Choi, Y. S. Youn, J. Choi, T. H. Kang, M. C. Jung, H. J. Shin, H. J. Lee, S. Kim and B. Kim, Scanning Photoemission Microscopy of Graphene Sheets on SiO₂, *Adv. Mater.*, 2008, **20**, 3589–91.

87 H. Hibino, H. Kageshima, M. Kotsugi, F. Maeda, F.-Z. Guo and Y. Watanabe, Dependence of electronic properties of epitaxial few-layer graphene on the number of layers investigated by photoelectron emission microscopy, *Phys. Rev. B: Condens. Matter Mater. Phys. Mater. Phys.: Condens. Matter*, 2009, **79**, 125431.

88 H. Y. Mao, R. Wang, H. Huang, Y. Z. Wang, X. Y. Gao, S. N. Bao, A. T. S. Wee and W. Chen, Tuning of C[sub 60] energy levels using orientation-controlled phthalocyanine films, *J. Appl. Phys.*, 2010, **108**, 053706–6.

89 C. Q. Sun, Dominance of broken bonds and nonbonding electrons at the nanoscale, *Nanoscale*, 2010, **2**, 1930–61.

90 C. Q. Sun, Size dependence of nanostructures: Impact of bond order deficiency, *Prog. Solid State Chem.*, 2007, **35**, 1–159.

91 V. M. Goldschmidt, Crystal structure and chemical correlation, *Berichte Der Deutschen Chemischen Gesellschaft*, 1927, **60**, 1263–96.

92 L. Pauling, Atomic radii and interatomic distances in metals, *J. Am. Chem. Soc.*, 1947, **69**, 542–53.

93 P. J. Feibelman, Relaxation of hcp(0001) surfaces: A chemical view, *Phys. Rev. B: Condens. Matter Mater. Phys. Mater. Phys.: Condens. Matter*, 1996, **53**, 13740–6.

94 C. Q. Sun, Thermo-mechanical behavior of low-dimensional systems: The local bond average approach, *Prog. Mater. Sci.*, 2009, **54**, 179–307.

95 C. Q. Sun, H. L. Bai, B. K. Tay, S. Li and E. Y. Jiang, Dimension, strength, and chemical and thermal stability of a single C–C bond in carbon nanotubes, *J. Phys. Chem. B*, 2003, **107**, 7544–6.

96 X. Zhang, J.-l. Kuo, M. Gu, P. Bai and C. Q. Sun, Graphene nanoribbon band-gap expansion: Broken-bond-induced edge strain and quantum entrapment, *Nanoscale*, 2010, **2**, 2160–3.

97 X. J. Liu, J. W. Li, Z. F. Zhou, L. W. Yang, Z. S. Ma, G. F. Xie, Y. Pan and C. Q. Sun, Size-induced elastic stiffening of ZnO nanostructures: Skin-depth energy pinning, *Appl. Phys. Lett.*, 2009, **94**, 131902.

98 C. Q. Sun, Y. Wang, B. K. Tay, S. Li, H. Huang and Y. B. Zhang, Correlation between the melting point of a nanosolid and the cohesive energy of a surface atom, *J. Phys. Chem. B*, 2002, **106**, 10701–5.

99 M. X. Gu, C. Q. Sun, C. M. Tan and S. Z. Wang, Local bond average for the size and temperature dependence of elastic and vibronic properties of nanostructures, *International Journal of Nanotechnology*, 2009, **6**, 640–52.

100 M. A. Omar, *Elementary Solid State Physics: Principles and Applications*. 1993, New York: Addison-Wesley.

101 Y. Wang, L. L. Wang and C. Q. Sun, The 2p₃/₂ binding energy shift of Fe surface and Fe nanoparticles, *Chem. Phys. Lett.*, 2009, **480**, 243–6.

102 I. Aruna, B. R. Mehta, L. K. Malhotra and S. M. Shivaprasad, Size dependence of core and valence binding energies in Pd nanoparticles: Interplay of quantum confinement and coordination reduction, *J. Appl. Phys.*, 2008, **104**, 064308.

103 B. Balamurugan and T. Maruyama, Inhomogeneous effect of particle size on core-level and valence-band electrons: Size-dependent electronic structure of Cu3N nanoparticles, *Appl. Phys. Lett.*, 2006, **89**, 033112.

104 S. P. Suprun and E. V. Fedosenko, Low-temperature recrystallization of Ge nanolayers on ZnSe, *Semiconductors*, 2007, **41**, 590–5.

105 Y. Wang, Y. G. Nie, J. S. Pan, L. K. Pan, Z. Sun, L. L. Wang and C. Q. Sun, Orientation-resolved 3d(5/2) binding energy shift of Rh and Pd surfaces: anisotropy of the skin-depth lattice strain and quantum trapping, *PCCP*, 2010, **12**, 2177–82.

106 Y. Wang, Y. G. Nie, L. L. Wang and C. Q. Sun, Atomic-Layer- and Crystal-Orientation-Resolved 3d₅/₂ Binding Energy Shift of Ru(0001) and Ru(1010) Surfaces, *J Chem Phys C*, 2010, **114**, 1226–30.

652 | *Energy Environ. Sci.*, 2011, **4**, 627–655

This journal is © The Royal Society of Chemistry 2011

107 C. Q. Sun, Oxidation electronics: bond-band-barrier correlation and its applications, *Prog. Mater. Sci.*, 2003, **48**, 521–685.

108 C. Q. Sun, Y. Sun, Y. G. Nie, Y. Wang, J. S. Pan, G. Ouyang, L. K. Pan and Z. Sun, 1s Binding Energy of Carbon Allotropes and the Effective Atomic Coordination of the Few-Layer Graphene, *J Chem Phys C*, 2009, **113**, 16464–7.

109 R. A. Street, *Hydrogenated amorphous silicon*. 1991: Cambridge University Press.

110 P. W. Atkins, *Physical Chemistry*. 4 ed. 1990: Oxford University Press.

111 W. T. Zheng and C. Q. Sun, Electronic process of nitriding: Mechanism and applications, *Prog. Solid State Chem.*, 2006, **34**, 1–20.

112 T. Ohta, A. Bostwick, T. Seyller, K. Horn and E. Rotenberg, Controlling the electronic structure of bilayer graphene, *Science*, 2006, **313**, 951–4.

113 C. Q. Sun, Y. G. Nie, J. S. Pan and W. T. Zheng, Graphitic Dirac-Fermi polarons generation and purification, *Communicated*, 2010.

114 O. Volnianska and P. Boguslawski, Magnetism of solids resulting from spin polarization of p orbitals, *J. Phys.: Condens. Matter*, 2010, **22**, 073202.

115 K. A. Ritter and J. W. Lyding, The influence of edge structure on the electronic properties of graphene quantum dots and nanoribbons, *Nat. Mater.*, 2009, **8**, 235–42.

116 H. Beckmann and G. Bergmann, Magnetism of Rh and Ru atoms, clusters, and monolayers on Au and Ag surfaces, *Phys. Rev. B: Condens. Matter Mater. Phys. Mater. Phys.: Condens. Matter*, 1997, **55**, 14350–9.

117 E. W. Wong, P. E. Sheehan and C. M. Lieber, Nanobeam mechanics: Elasticity, strength, and toughness of nanorods and nanotubes, *Science*, 1997, **277**, 1971–5.

118 G. Zhang and B. W. Li, Wall "thickness" effects on Raman spectrum shift, thermal conductivity, and Young's modulus of single-walled nanotubes, *J. Phys. Chem. B*, 2005, **109**, 23823–6.

119 X. Zhou, J. J. Zhou and Z. C. Ou-Yang, Strain energy and Young's modulus of single-wall carbon nanotubes calculated from electronic energy-band theory, *Phys. Rev. B: Condens. Matter Mater. Phys. Mater. Phys.: Condens. Matter*, 2000, **62**, 13692–6.

120 C. Lee, X. D. Wei, J. W. Kysar and J. Hone, Measurement of the elastic properties and intrinsic strength of monolayer graphene, *Science*, 2008, **321**, 385–8.

121 E. Cadelano, P. L. Palla, S. Giordano and L. Colombo, Nonlinear Elasticity of Monolayer Graphene, *Phys. Rev. Lett.*, 2009, **102**, 235502.

122 J. Li, Z. Li, G. Zhou, Z. Liu, J. Wu, B.-L. Gu, J. Ihm and W. Duan, Spontaneous edge-defect formation and defect-induced conductance suppression in graphene nanoribbons, *Phys. Rev. B: Condens. Matter Mater. Phys. Mater. Phys.: Condens. Matter*, 2010, **82**, 115410.

123 M. Terrones, H. Terrones, F. Banhart, J. C. Charlier and P. M. Ajayan, Coalescence of single-walled carbon nanotubes, *Science*, 2000, **288**, 1226–9.

124 K. Metenier, S. Bonnamy, F. Beguin, C. Journet, P. Bernier, M. L. de La Chapelle, O. Chauvet and S. Lefrant, Coalescence of single-walled carbon nanotubes and formation of multi-walled carbon nanotubes under high-temperature treatments, *Carbon*, 2002, **40**, 1765–73.

125 R. Andrews, D. Jacques, D. Qian and E. C. Dickey, Purification and structural annealing of multiwalled carbon nanotubes at graphitization temperatures, *Carbon*, 2001, **39**, 1681–7.

126 D. Bom, R. Andrews, D. Jacques, J. Anthony, B. L. Chen, M. S. Meier and J. P. Selegue, Thermogravimetric analysis of the oxidation of multiwalled carbon nanotubes: Evidence for the role of defect sites in carbon nanotube chemistry, *Nano Lett.*, 2002, **2**, 615–9.

127 S. Bandow, S. Asaka, Y. Saito, A. M. Rao, L. Grigorian, E. Richter and P. C. Eklund, Effect of the growth temperature on the diameter distribution and chirality of single-wall carbon nanotubes, *Phys. Rev. Lett.*, 1998, **80**, 3779–82.

128 R. E. Miller and V. B. Shenoy, Size-dependent elastic properties of nanosized structural elements, *Nanotechnology*, 2000, **11**, 139–47.

129 C. Q. Sun, B. K. Tay, S. P. Lau, X. W. Sun, X. T. Zeng, S. Li, H. L. Bai, H. Liu, Z. H. Liu and E. Y. Jiang, Bond contraction and lone pair interaction at nitride surfaces, *J. Appl. Phys.*, 2001, **90**, 2615–7.

130 T. Halicioglu, Calculation of surface energies for low index planes of diamond, *Surf. Sci.*, 1991, **259**, L714–L8.

131 F. Scarpa, S. Adhikari and R. Chowdhury, The transverse elasticity of bilayer graphene, *Phys. Lett. A*, 2010, **374**, 2053–7.

132 F. Scarpa, S. Adhikari, A. J. Gil and C. Remillat, The bending of single layer graphene sheets: the lattice *versus* continuum approach, *Nanotechnology*, 2010, **21**, 125702.

133 P. Bennich, C. Puglia, P. A. Bruhwiler, A. Nilsson, A. J. Maxwell, A. Sandell, N. Martensson and P. Rudolf, Photoemission study of K on graphite, *Phys. Rev. B: Condens. Matter Mater. Phys. Mater. Phys.: Condens. Matter*, 1999, **59**, 8292–304.

134 C. S. Yannoni, P. P. Bernier, D. S. Bethune, G. Meijer and J. R. Salem, NMR DETERMINATION OF THE BOND LENGTHS IN C60, *J. Am. Chem. Soc.*, 1991, **113**, 3190–2.

135 K. V. Emtsev, F. Speck, T. Seyller, L. Ley and J. D. Riley, Interaction, growth, and ordering of epitaxial graphene on SiC{0001} surfaces: A comparative photoelectron spectroscopy study, *Phys. Rev. B: Condens. Matter Mater. Phys. Mater. Phys.: Condens. Matter*, 2008, **77**, 155303.

136 A. Stacey, B. C. C. Cowie, J. Orwa, S. Prawer and A. Hoffman, Diamond C 1s core-level excitons: Surface sensitivity, *Phys. Rev. B: Condens. Matter Mater. Phys. Mater. Phys.: Condens. Matter*, 2010, **82**, 125427.

137 S. Lizzit, G. Zampieri, L. Petaccia, R. Larciprete, P. Lacovig, E. D. L. Rienks, G. Bihlmayer, A. Baraldi and P. Hofmann, Band dispersion in the deep 1s core level of graphene, *Nat. Phys.*, 2010, **6**, 345–9.

138 U. Starke and C. Riedl, Epitaxial graphene on SiC(0001) and SiC(000(1)over-bar): from surface reconstructions to carbon electronics, *J. Phys.: Condens. Matter*, 2009, **21**, 134016.

139 T. Filleter, K. V. Emtsev, T. Seyller and R. Bennewitz, Local work function measurements of epitaxial graphene, *Appl. Phys. Lett.*, 2008, **93**, 133117.

140 T. Balasubramanian, J. N. Andersen and L. Wallden, Surface-bulk core-level splitting in graphite, *Phys. Rev. B: Condens. Matter Mater. Phys. Mater. Phys.: Condens. Matter*, 2001, **64**, 205420.

141 Y. M. Shulga, T. C. Tien, C. C. Huang, S. C. Lo, V. Muradyan, N. V. Polyakova, Y. C. Ling, R. O. Loutfy and A. P. Moravsky, XPS study of fluorinated carbon multi-walled nanotubes, *J. Electron Spectrosc. Relat. Phenom.*, 2007, **160**, 22–8.

142 A. Goldoni, R. Larciprete, L. Gregoratti, B. Kaulich, M. Kiskinova, Y. Zhang, H. Dai, L. Sangaletti and F. Parmigiani, X-ray photoelectron microscopy of the C 1s core level of free-standing single-wall carbon nanotube bundles, *Appl. Phys. Lett.*, 2002, **80**, 2165–7.

143 G. Speranza and N. Laidani, Measurement of the relative abundance of sp(2) and sp(3) hybridised atoms in carbon based materials by XPS: a critical approach. Part I, *Diamond Relat. Mater.*, 2004, **13**, 445–50.

144 S. Takabayashi, K. Motomitsu, T. Takahagi, A. Terayama, K. Okamoto and T. Nakatani, Qualitative analysis of a diamondlike carbon film by angle-resolved x-ray photoelectron spectroscopy, *J. Appl. Phys.*, 2007, **101**, 103542.

145 K. G. Saw and J. du Plessis, The X-ray photoelectron spectroscopy C 1s diamond peak of chemical vapour deposition diamond from a sharp interfacial structure, *Mater. Lett.*, 2004, **58**, 1344–8.

146 W. T. Zheng, C. Q. Sun and B. K. Tay, Modulating the work function of carbon by N or O addition and nanotip fabrication, *Solid State Commun.*, 2003, **128**, 381–4.

147 Z. Osvath, G. Vertesy, L. Tapaszto, F. Weber, Z. E. Horvath, J. Gyulai and L. P. Biro, Scanning tunneling microscopy investigation of atomic-scale carbon nanotube defects produced by Ar+ ion irradiation, *Materials Science & Engineering C-Biomimetic and Supramolecular Systems*, 2006, **26**, 1194–7.

148 Y. Ferro and A. Allouche, Interpretation of STM images of graphite with an atomic vacancy *via* density-functional calculations of electronic structure, *Phys. Rev. B: Condens. Matter Mater. Phys. Mater. Phys.: Condens. Matter*, 2007, **75**, 155438.

149 Y. B. Zhang, V. W. Brar, C. Girit, A. Zettl and M. F. Crommie, Origin of spatial charge inhomogeneity in graphene, *Nat. Phys.*, 2009, **5**, 722–6.

150 G. Speranza and L. Minati, The surface and bulk core line's in crystalline and disordered polycrystalline graphite, *Surf. Sci.*, 2006, **600**, 4438–44.

151 C. Q. Sun, Y. Wang, Y. G. Nie, Y. Sun, J. S. Pan, L. K. Pan and Z. Sun, Adatoms-Induced Local Bond Contraction, Quantum Trap Depression, and Charge Polarization at Pt and Rh Surfaces, *J Chem Phys C*, 2009, **113**, 21889–94.

152 P. Czoschke, H. W. Hong, L. Basile and T. C. Chiang, Quantum oscillations in the layer structure of thin metal films, *Phys. Rev. Lett.*, 2003, **91**, 226801.

153 K. Ostrikov, Colloquium: Reactive plasmas as a versatile nanofabrication tool, *Rev. Mod. Phys.*, 2005, **77**, 489–511.

154 K. Y. Wu, W. Y. Chen, J. Hwang, H. K. Wei, C. S. Kou, C. Y. Lee, Y. L. Liu and H. Y. Huang, Structure modification of highly ordered pyrolytic graphite by Ar plasma beam scanning at different incident angles, *Applied Physics a-Materials Science & Processing*, 2009, **95**, 707–12.

155 D. Q. Yang and E. Sacher, s-p hybridization in highly oriented pyrolytic graphite and its change on surface modification, as studied by X-ray photoelectron and Raman spectroscopies, *Surf. Sci.*, 2002, **504**, 125–37.

156 C. Q. Sun, Y. Wang, Y. G. Nie, B. R. Mehta, M. Khanuja, S. M. Shivaprasad, Y. Sun, J. S. Pan, L. K. Pan and Z. Sun, Interface quantum trap depression and charge polarization in the CuPd and AgPd bimetallic alloy catalysts, *PPhys. Chem. Chem. Phys.*, 2010, **12**, 3131–5.

157 Y. B. Zhang, T. T. Tang, C. Girit, Z. Hao, M. C. Martin, A. Zettl, M. F. Crommie, Y. R. Shen and F. Wang, Direct observation of a widely tunable bandgap in bilayer graphene, *Nature*, 2009, **459**, 820–3.

158 L. Liu and Z. Shen, Bandgap engineering of graphene: A density functional theory study, *Appl. Phys. Lett.*, 2009, **95**, 252104–3.

159 F. Zheng, K. i. Sasaki, R. Saito, W. Duan and B. L. Gu, Edge States of Zigzag Boron Nitride Nanoribbons, *J. Phys. Soc. Jpn.*, 2009, **78**, 074713.

160 D. Finkenstadt, G. Pennington and M. J. Mehl, From graphene to graphite: A general tight-binding approach for nanoribbon carrier transport, *Phys. Rev. B: Condens. Matter Mater. Phys. Mater. Phys.: Condens. Matter*, 2007, **76**, 121405.

161 D. Gunlycke, D. A. Areshkin and C. T. White, Semiconducting graphene nanostrips with edge disorder, *Appl. Phys. Lett.*, 2007, **90**, 142104.

162 T. C. Li and S. P. Lu, Quantum conductance of graphene nanoribbons with edge defects, *Phys. Rev. B: Condens. Matter Mater. Phys. Mater. Phys.: Condens. Matter*, 2008, **77**, 085408.

163 B. Zheng, P. Hermet and L. Henrard, Scanning Tunneling Microscopy Simulations of Nitrogen- and Boron-Doped Graphene and Single-Walled Carbon Nanotubes, *Acs Nano*, 2010, **4**, 4165–73.

164 S. S. Yu, W. T. Zheng, Q. B. Wen and Q. Jiang, First principle calculations of the electronic properties of nitrogen-doped carbon nanoribbons with zigzag edges, *Carbon*, 2008, **46**, 537–43.

165 S. S. Yu, W. T. Zheng and Q. Jiang, Oxidation of Graphene Nanoribbon by Molecular Oxygen, *IEEE Trans. Nanotechnol.ology*, 2008, **7**, 628–35.

166 D. Gunlycke, J. Li, J. W. Mintmire and C. T. White, Edges Bring New Dimension to Graphene Nanoribbons, *Nano Lett.*, 2010, **10**, 3638–42.

167 Y. Ren and K. Q. Chen, Effects of symmetry and Stone-Wales defect on spin-dependent electronic transport in zigzag graphene nanoribbons, *J. Appl. Phys.*, 2010, **107**, 044514.

168 Y. Ren, K. Q. Chen, Q. Wan, B. S. Zou and Y. Zhang, Transitions between semiconductor and metal induced by mixed deformation in carbon nanotube devices, *Appl. Phys. Lett.*, 2009, **94**, 183506.

169 Y. E. Xie, Y. P. Chen and J. X. Zhong, Electron transport of folded graphene nanoribbons, *J. Appl. Phys.*, 2009, **106**, 103714.

170 W. Zhang, L. Sun, Z. Xu, A. V. Krasheninnikov, P. Huai, Z. Zhu and F. Banhart, Migration of gold atoms in graphene ribbons: Role of the edges, *Phys. Rev. B: Condens. Matter Mater. Phys. Mater. Phys.: Condens. Matter*, 2010, **81**, 125425.

171 V. Barone, O. Hod and G. E. Scuseria, Electronic Structure and Stability of Semiconducting Graphene Nanoribbons, *Nano Lett.*, 2006, **6**, 2748–54.

172 T. Fujita, Y. Okawa, Y. Matsumoto and K. Tanaka, Phase boundaries of nanometer scale c(2x2)–O domains on the Cu(100) surface, *Phys. Rev. B: Condens. Matter Mater. Phys. Mater. Phys.: Condens. Matter*, 1996, **54**, 2167–74.

173 S. Okada and A. Oshiyama, Magnetic Ordering in Hexagonally Bonded Sheets with First-Row Elements, *Phys. Rev. Lett.*, 2001, **87**, 146803.

174 H. Lee, Y.-W. Son, N. Park, S. Han and J. Yu, Magnetic ordering at the edges of graphitic fragments: Magnetic tail interactions between the edge-localized states, *Phys. Rev. B: Condens. Matter Mater. Phys. Mater. Phys.: Condens. Matter*, 2005, **72**, 174431.

175 Z. Zanolli and J. C. Charlier, Spin transport in carbon nanotubes with magnetic vacancy-defects, *Phys. Rev. B: Condens. Matter Mater. Phys. Mater. Phys.: Condens. Matter*, 2010, **81**, 165406.

176 B. Xu, J. Yin, Y. D. Xia, X. G. Wan, K. Jiang and Z. G. Liu, Electronic and magnetic properties of zigzag graphene nanoribbon with one edge saturated, *Appl. Phys. Lett.*, 2010, **96**, 163102.

177 S. Ma, J. H. Xia, V. Srikanth, X. Sun, T. Staedler, X. Jiang, F. Yang and Z. D. Zhang, Magnetism of amorphous carbon nanofibers, *Appl. Phys. Lett.*, 2009, **95**, 263105.

178 M. P. Lopez-Sancho, F. de Juan and M. A. H. Vozmediano, Magnetic moments in the presence of topological defects in graphene, *Phys. Rev. B: Condens. Matter Mater. Phys. Mater. Phys.: Condens. Matter*, 2009, **79**, 075413.

179 S. S. Alexandre, M. S. C. Mazzoni and H. Chacham, Edge states and magnetism in carbon nanotubes with line defects, *Phys. Rev. Lett.*, 2008, **100**, 146801.

180 J. J. Palacios, J. Fernandez-Rossier and L. Brey, Vacancy-induced magnetism in graphene and graphene ribbons, *Phys. Rev. B: Condens. Matter Mater. Phys. Mater. Phys.: Condens. Matter*, 2008, **77**, 195428.

181 S. Bhowmick and V. B. Shenoy, Edge state magnetism of single layer graphene nanostructures, *J. Chem. Phys.*, 2008, **128**, 244717.

182 Y. Wang, Y. Huang, Y. Song, X. Y. Zhang, Y. F. Ma, J. J. Liang and Y. S. Chen, Room-Temperature Ferromagnetism of Graphene, *Nano Lett.*, 2009, **9**, 220–4.

183 V. L. J. Joly, M. Kiguchi, S.-J. Hao, K. Takai, T. Enoki, R. Sumii, K. Amemiya, H. Muramatsu, T. Hayashi, Y. A. Kim, M. Endo, J. Campos-Delgado, F. Lopez-Urias, A. Botello-Mendez, H. Terrones, M. Terrones and M. S. Dresselhaus, Observation of magnetic edge state in graphene nanoribbons, *Phys. Rev. B: Condens. Matter Mater. Phys. Mater. Phys.*, 2010, **81**, 245428.

184 P. O. Lehtinen, A. S. Foster, Y. Ma, A. V. Krasheninnikov and R. M. Nieminen, Irradiation-Induced Magnetism in Graphite: A Density Functional Study, *Phys. Rev. Lett.*, 2004, **93**, 187202.

185 O. V. Yazyev and L. Helm, Defect-induced magnetism in graphene, *Phys. Rev. B: Condens. Matter Mater. Phys. Mater. Phys.*, 2007, **75**, 125408.

186 Y. Kobayashi, K. Fukui, T. Enoki and K. Kusakabe, Edge state on hydrogen-terminated graphite edges investigated by scanning tunneling microscopy, *Phys. Rev. B: Condens. Matter Mater. Phys. Mater. Phys.: Condens. Matter*, 2006, **73**, 125415.

187 B. Huang, Y. W. Son, G. Kim, W. H. Duan and J. Ihm, Electronic and Magnetic Properties of Partially Open Carbon Nanotubes, *J. Am. Chem. Soc.*, 2009, **131**, 17919–25.

188 E. H. Lieb, Two theorems on the Hubbard model, *Phys. Rev. Lett.*, 1989, **62**, 1201.

189 X. M. Yang, H. H. Xia, X. B. Qin, W. F. Li, Y. Y. Dai, X. D. Liu, M. W. Zhao, Y. Y. Xia, S. S. Yan and B. Y. Wang, Correlation between the vacancy defects and ferromagnetism in graphite, *Carbon*, 2009, **47**, 1399–406.

190 O. V. Yazyev, Magnetism in disordered graphene and irradiated graphite, *Phys. Rev. Lett.*, 2008, **101**, 037203.

191 R. Singh and P. Kroll, Magnetism in graphene due to single-atom defects: dependence on the concentration and packing geometry of defects, *J. Phys.: Condens. Matter*, 2009, **21**, 196002.

192 E. B. Sonin, Edge accumulation and currents of moment in two-dimensional topological insulators, *Phys. Rev. B: Condens. Matter Mater. Phys. Mater. Phys.: Condens. Matter*, 2010, **82**, 113307.

193 B. Delley, An all-electron numerical-method for solving the local density functional for polyatomic-molecules, *J. Chem. Phys.*, 1990, **92**, 508–17.

194 J. P. Perdew, K. Burke and M. Ernzerhof, Generalized gradient approximation made simple, *Phys. Rev. Lett.*, 1996, **77**, 3865–8.

195 D. Porezag, T. Frauenheim, T. Koler, G. Seifert and R. Kaschner, Construction of tight-binding-like potentials on the basis of density-functional theory: Application to carbon, *Phys. Rev. B: Condens. Matter Mater. Phys. Mater. Phys.*, 1995, **51**, 12947.

196 M. P. Lima, A. J. R. da Silva and A. Fazzio, Splitting of the zero-energy edge states in bilayer graphene, *Phys. Rev. B: Condens. Matter Mater. Phys. Mater. Phys.: Condens. Matter*, 2010, **81**, 045430.

197 B. Tang, G. X. Hu and H. Y. Gao, Raman Spectroscopic Characterization of Graphene, *Appl. Spectrosc. Rev.*, 2010, **45**, 369–407.

198 L. M. Malard, M. A. Pimenta, G. Dresselhaus and M. S. Dresselhaus, Raman spectroscopy in graphene, *Physics Reports-Review Section of Physics Letters*, 2009, **473**, 51–87.

199 Y. H. Wu, T. Yu and Z. X. Shen, Two-dimensional carbon nanostructures: Fundamental properties, synthesis, characterization, and potential applications, *J. Appl. Phys.*, 2010, **108**, 071301–38.

200 Y. F. Hao, Y. Y. Wang, L. Wang, Z. H. Ni, Z. Q. Wang, R. Wang, C. K. Koo, Z. X. Shen and J. T. L. Thong, Probing Layer Number and Stacking Order of Few-Layer Graphene by Raman Spectroscopy, *Small*, 2010, **6**, 195–200.

201 H. Wang, Y. F. Wang, X. W. Cao, M. Feng and G. X. Lan, Vibrational properties of graphene and graphene layers, *J. Raman Spectrosc.*, 2009, **40**, 1791–6.

202 A. Gupta, G. Chen, P. Joshi, S. Tadigadapa and P. C. Eklund, Raman scattering from high-frequency phonons in supported n-graphene layer films, *Nano Lett.*, 2006, **6**, 2667–73.

203 D. Graf, F. Molitor, K. Ensslin, C. Stampfer, A. Jungen, C. Hierold and L. Wirtz, Spatially resolved raman spectroscopy of single- and few-layer graphene, *Nano Lett.*, 2007, **7**, 238–42.

204 T. Yu, Z. H. Ni, C. L. Du, Y. M. You, Y. Y. Wang and Z. X. Shen, Raman mapping investigation of graphene on transparent flexible substrate: The strain effect, *J Chem Phys C*, 2008, **112**, 12602–5.

205 T. M. G. Mohiuddin, A. Lombardo, R. R. Nair, A. Bonetti, G. Savini, R. Jalil, N. Bonini, D. M. Basko, C. Galiotis, N. Marzari, K. S. Novoselov, A. K. Geim and A. C. Ferrari, Uniaxial strain in graphene by Raman spectroscopy: G peak splitting, Gruneisen parameters, and sample orientation, *Phys. Rev. B: Condens. Matter Mater. Phys. Mater. Phys.: Condens. Matter*, 2009, **79**, 205433.

206 M. Huang, H. Yan, T. F. Heinz and J. Hone, Probing Strain-Induced Electronic Structure Change in Graphene by Raman Spectroscopy, *Nano Lett.*, 2010, **10**, 4074–9.

207 I. Calizo, S. Ghosh, W. Bao, F. Miao, C. Ning Lau and A. A. Balandin, Raman nanometrology of graphene: Temperature and substrate effects, *Solid State Commun.*, 2009, **149**, 1132–5.

208 Y. M. You, Z. H. Ni, T. Yu and Z. X. Shen, Edge chirality determination of graphene by Raman spectroscopy, *Appl. Phys. Lett.*, 2008, **93**, 163112.

209 B. Krauss, P. t. Nemes-Incze, V. Skakalova, L. s. P. Biro, K. v. Klitzing and J. H. Smet, Raman Scattering at Pure Graphene Zigzag Edges, *Nano Lett.*, 2010: null-null.

210 A. K. Gupta, T. J. Russin, H. R. Gutieérrez and P. C. Eklund, Probing Graphene Edges *via* Raman Scattering, *Acs Nano*, 2008, **3**, 45–52.

211 E. H. Martins Ferreira, M. V. O. Moutinho, F. Stavale, M. M. Lucchese, R. B. Capaz, C. A. Achete and A. Jorio, Evolution of the Raman spectra from single-, few-, and many-layer graphene with increasing disorder, *Phys. Rev. B: Condens. Matter Mater. Phys. Mater. Phys.: Condens. Matter*, 2010, **82**, 125429.

212 S. p. Berciaud, S. Ryu, L. E. Brus and T. F. Heinz, Probing the Intrinsic Properties of Exfoliated Graphene: Raman Spectroscopy of Free-Standing Monolayers, *Nano Lett.*, 2008, **9**, 346–52.

213 Z. Q. Luo, T. Yu, K. J. Kim, Z. H. Ni, Y. M. You, S. Lim, Z. X. Shen, S. Z. Wang and J. Y. Lin, Thickness-Dependent Reversible Hydrogenation of Graphene Layers, *Acs Nano*, 2009, **3**, 1781–8.

214 L. G. Cancado, M. A. Pimenta, B. R. A. Neves, M. S. S. Dantas and A. Jorio, Influence of the atomic structure on the Raman spectra of graphite edges, *Phys. Rev. Lett.*, 2004, **93**, 247401.

215 M. A. Pimenta, G. Dresselhaus, M. S. Dresselhaus, L. G. Cancado, A. Jorio and R. Saito, Studying disorder in graphite-based systems by Raman spectroscopy, *PCCP*, 2007, **9**, 1276–90.

216 M. S. Dresselhaus, A. Jorio, and R. Saito, Characterizing Graphene, Graphite, and Carbon Nanotubes by Raman Spectroscopy, in *Annual Review of Condensed Matter Physics*, Vol. 1. 2010. p. 89–108.

217 M. Y. Huang, H. G. Yan, C. Y. Chen, D. H. Song, T. F. Heinz, and J. Hone, Phonon softening and crystallographic orientation of strained graphene studied by Raman spectroscopy. *Proceedings of the National Academy of Sciences of the United States of America*, 2009. 106: 7304–8.

218 Z. H. Ni, T. Yu, Y. H. Lu, Y. Y. Wang, Y. P. Feng and Z. X. Shen, Uniaxial Strain on Graphene: Raman Spectroscopy Study and Band-Gap Opening, *Acs Nano*, 2008, **2**, 2301–5.

219 C. Q. Sun, L. K. Pan, C. M. Li and S. Li, Size-induced acoustic hardening and optic softening of phonons in InP, CeO2, SnO2, CdS, Ag, and Si nanostructures, *Phys. Rev. B: Condens. Matter Mater. Phys. Mater. Phys.: Condens. Matter*, 2005, **72**, 134301.

220 L. K. Pan, C. Q. Sun and C. M. Li, Elucidating Si–Si dimmer vibration from the size-dependent Raman shift of nanosolid Si, *J. Phys. Chem. B*, 2004, **108**, 3404–6.

221 M. X. Gu, Y. C. Zhou and C. Q. Sun, Local bond average for the thermally induced lattice expansion, *J. Phys. Chem. B*, 2008, **112**, 7992–5.

222 M. X. Gu, Y. C. Zhou, L. K. Pan, Z. Sun, S. Z. Wang and C. Q. Sun, Temperature dependence of the elastic and vibronic behavior of Si, Ge, and diamond crystals, *J. Appl. Phys.*, 2007, **102**, 083524.

223 M. X. Gu, C. Q. Sun, Z. Chen, T. C. A. Yeung, S. Li, C. M. Tan and V. Nosik, Size, temperature, and bond nature dependence of elasticity and its derivatives on extensibility, Debye temperature, and heat capacity of nanostructures, *Phys. Rev. B: Condens. Matter Mater. Phys. Mater. Phys.: Condens. Matter*, 2007, **75**, 125403.

224 M. X. Gu, L. K. Pan, T. C. A. Yeung, B. K. Tay and C. Q. Sun, Atomistic origin of the thermally driven softening of Raman optical phonons in group III nitrides, *J Chem Phys C*, 2007, **111**, 13606–10.

225 M. X. Gu, L. K. Pan, B. K. Tay and C. Q. Sun, Atomistic origin and temperature dependence of Raman optical redshift in nanostructures: a broken bond rule, *J. Raman Spectrosc.*, 2007, **38**, 780–8.

226 L. Limot, E. Pehlke, J. Kroger and R. Berndt, Surface-state localization at adatoms, *Phys. Rev. Lett.*, 2005, **94**, 036805.

227 J. N. Crain and D. T. Pierce, End states in one-dimensional atom chains, *Science*, 2005, **307**, 703–6.

228 V. S. Stepanyuk, A. N. Klavsyuk, L. Niebergall and P. Bruno, End electronic states in Cu chains on Cu(111): Ab initio calculations, *Phys. Rev. B: Condens. Matter Mater. Phys. Mater. Phys.: Condens. Matter*, 2005, **72**, 153407.

229 S. S. Yu and W. T. Zheng, Effect of N/B doping on the electronic and field emission properties for carbon nanotubes, carbon nanocones, and graphene nanoribbons, *Nanoscale*, 2010, **2**, 1069–82.

230 X. Y. Hu, H. W. Tian, W. T. Zheng, S. S. Yu, L. Qiao, C. Q. Qu and Q. Jiang, Metallic-semiconducting phase transition of the edge-oxygenated armchair graphene nanoribbons, *Chem. Phys. Lett.*, 2010, **501**(1–3), 64–67.

231 U. A. Palnitkar, R. V. Kashid, M. A. More, D. S. Joag, L. S. Panchakarla and C. N. R. Rao, Remarkably low turn-on field emission in undoped, nitrogen-doped, and boron-doped graphene, *Appl. Phys. Lett.*, 2010, **97**, 063102.

232 W. T. Zheng, Y. M. Ho, H. W. Tian, M. Wen, J. L. Qi and Y. A. Li, Field Emission from a Composite of Graphene Sheets and ZnO Nanowires, *J Chem Phys C*, 2009, **113**, 9164–8.

233 A. Malesevic, R. Kemps, A. Vanhulsel, M. P. Chowdhury, A. Volodin and C. Van Haesendonck, Field emission from vertically aligned few-layer graphene, *J. Appl. Phys.*, 2008, **104**, 084301.

234 R. Grantab, V. B. Shenoy and R. S. Ruoff, Anomalous Strength Characteristics of Tilt Grain Boundaries in Graphene, *Science*, 2010, **330**, 946–948.

235 C. Kittel, *Introduction to Solid State Physics*, John Wiley & Sons Inc., New York, 8th edn, 2005.